

*Fast and slow shifts of the zonal-mean
intertropical convergence zone in
response to an idealized anthropogenic
aerosol*

Article

Published Version

Creative Commons: Attribution-Noncommercial-No Derivative Works 4.0

Open access

Voigt, A., Pincus, R., Stevens, B., Bony, S., Boucher, O., Bellouin, N. ORCID: <https://orcid.org/0000-0003-2109-9559>, Lewinschal, A., Medeiros, B., Wang, Z. and Zhang, H. (2017) Fast and slow shifts of the zonal-mean intertropical convergence zone in response to an idealized anthropogenic aerosol. *Journal of Advances in Modeling Earth Systems*, 9 (2). pp. 870-892. ISSN 1942-2466 doi: <https://doi.org/10.1002/2016MS000902> Available at <https://centaur.reading.ac.uk/70183/>

It is advisable to refer to the publisher's version if you intend to cite from the work. See [Guidance on citing](#).

Published version at: <http://onlinelibrary.wiley.com/doi/10.1002/2016MS000902/full>

To link to this article DOI: <http://dx.doi.org/10.1002/2016MS000902>

Publisher: American Geophysical Union

All outputs in CentAUR are protected by Intellectual Property Rights law, including copyright law. Copyright and IPR is retained by the creators or other copyright holders. Terms and conditions for use of this material are defined in

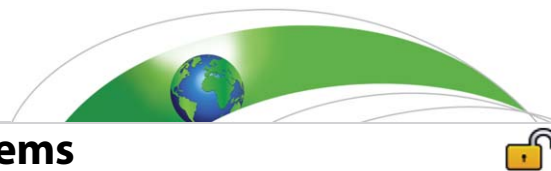
the [End User Agreement](#).

www.reading.ac.uk/centaur

CentAUR

Central Archive at the University of Reading

Reading's research outputs online



RESEARCH ARTICLE

10.1002/2016MS000902

Key Points:

- Fast and slow aerosol impacts oppose each other, but slow SST-mediated ITCZ shift is much larger
- Zonal aerosol distribution has little impact, and SST coupling makes the precipitation response more zonal
- Aerosol affects zonal-mean ITCZ, but impact is small and cloud uncertainty makes attribution difficult

Correspondence to:

A. Voigt,
aiko.voigt@kit.edu

Citation:

Voigt, A., R. Pincus, B. Stevens, S. Bony, O. Boucher, N. Bellouin, A. Lewinschal, B. Medeiros, Z. Whang, and H. Zhang (2017), Fast and slow shifts of the zonal-mean intertropical convergence zone in response to an idealized anthropogenic aerosol, *J. Adv. Model. Earth Syst.*, 9, doi:10.1002/2016MS000902.

Received 21 DEC 2016

Accepted 17 MAR 2017

Accepted article online 3 APR 2017

© 2017. The Authors.

This is an open access article under the terms of the Creative Commons Attribution-NonCommercial-NoDerivs License, which permits use and distribution in any medium, provided the original work is properly cited, the use is non-commercial and no modifications or adaptations are made.

Fast and slow shifts of the zonal-mean intertropical convergence zone in response to an idealized anthropogenic aerosol

Aiko Voigt^{1,2} , Robert Pincus^{3,4} , Bjorn Stevens⁵ , Sandrine Bony⁶ , Olivier Boucher⁶ , Nicolas Bellouin⁷ , Anna Lewinschal⁸, Brian Medeiros⁹ , Zhili Whang¹⁰ , and Hua Zhang¹¹ 

¹Karlsruhe Institute of Technology, Institute of Meteorology and Climate Research-Department Troposphere Research, Karlsruhe, Germany, ²Lamont-Doherty Earth Observatory, Columbia University, New York, New York, USA, ³Cooperative Institute for Research in Environmental Sciences, University of Colorado, Boulder, Colorado, USA, ⁴Physical Sciences Division, NOAA/Earth System Research Lab, Boulder, Colorado, USA, ⁵Max Planck Institute for Meteorology, Hamburg, Germany, ⁶LMD/IPSL, CNRS, Université Pierre et Marie Curie, Paris, France, ⁷Department of Meteorology, University of Reading, Reading, UK, ⁸Department of Meteorology and Bolin Centre for Climate Research, Stockholm University, Stockholm, Sweden, ⁹National Center for Atmospheric Research, Boulder, Colorado, USA, ¹⁰Chinese Academy of Meteorological Sciences, Beijing, China, ¹¹National Climate Center, China Meteorological Administration, Beijing, China

Abstract Previous modeling work showed that aerosol can affect the position of the tropical rain belt, i.e., the intertropical convergence zone (ITCZ). Yet it remains unclear which aspects of the aerosol impact are robust across models, and which are not. Here we present simulations with seven comprehensive atmosphere models that study the fast and slow impacts of an idealized anthropogenic aerosol on the zonal-mean ITCZ position. The fast impact, which results from aerosol atmospheric heating and land cooling before sea-surface temperature (SST) has time to respond, causes a northward ITCZ shift. Yet the fast impact is compensated locally by decreased evaporation over the ocean, and a clear northward shift is only found for an unrealistically large aerosol forcing. The local compensation implies that while models differ in atmospheric aerosol heating, this does not contribute to model differences in the ITCZ shift. The slow impact includes the aerosol impact on the ocean surface energy balance and is mediated by SST changes. The slow impact is an order of magnitude more effective than the fast impact and causes a clear southward ITCZ shift for realistic aerosol forcing. Models agree well on the slow ITCZ shift when perturbed with the same SST pattern. However, an energetic analysis suggests that the slow ITCZ shifts would be substantially more model-dependent in interactive-SST setups due to model differences in clear-sky radiative transfer and clouds. We also discuss implications for the representation of aerosol in climate models and attributions of recent observed ITCZ shifts to aerosol.

1. Introduction

Aerosol, particulate matter suspended in the atmosphere, has been implicated as a prime driver of observed past and projected future climate change. Aerosol interacts with radiation and clouds and, because its atmospheric residence time is limited to a few days, is concentrated near its emission regions. This spatial inhomogeneity might make aerosol particularly effective in impacting regional climate, i.e., the localized nature of the aerosol forcing can demand a circulation response even in the absence of regionally varying radiative feedbacks. This is in contrast to well-mixed greenhouse gases such as CO₂, which impacts the circulation largely via such feedbacks and the associated spatial patterns in the temperature response [e.g., Butler *et al.*, 2010; Ceppi *et al.*, 2014; Voigt and Shaw, 2015]. Despite the fact that the global-mean radiative forcing of aerosol is smaller than for CO₂, aerosol might thus be able to induce equally large or even larger circulation changes [Ming and Ramaswamy, 2011; Xie *et al.*, 2013]. A prominent example are the tropical rain belts, which have been argued to have shifted over the past century as a result of anthropogenic and natural aerosol change [Hwang *et al.*, 2013; Haywood *et al.*, 2013; Allen, 2015; Ridley *et al.*, 2015], and which are expected to shift northward over the course of the 21st century due to increasing CO₂ and decreasing anthropogenic aerosol [Frierson and Hwang, 2012; Friedman *et al.*, 2013; Allen, 2015].

Understanding the aerosol impact on the circulation, however, is a complicated task and involves problems that are largely absent for well-mixed greenhouse gases. First, aerosol is less constrained from observations than CO₂, and climate models often use different aerosol. This is true even in the coordinated efforts of the Phase 5 of the Coupled Model Intercomparison Project [Taylor et al., 2012]. Second, aerosol radiative forcing can be quite different between models even when models are forced with the same aerosol [Stier et al., 2013; Randles et al., 2013]. Aerosol forcing differences are usually more severe than for CO₂. Third, aerosol interacts with radiation and clouds, and these interactions can depend on the type of aerosol and clouds involved. Fourth, the aerosol's geographical and vertical distribution depends on small-scale aerosol formation and removal processes that are difficult to represent in global climate models. In fact, model studies of aerosol emission perturbations found that model differences in aerosol chemistry create large model differences in atmospheric aerosol loading [e.g., Myhre et al., 2013; Kasoar et al., 2016].

This suggests that progress might be made by separating the aerosol-circulation problem into a set of smaller subproblems that can be understood individually. A first step in building a hierarchical understanding is to force models with the same prescribed aerosol. In this paper we thus design an idealized anthropogenic aerosol and study its impact on the zonal-mean ITCZ position in an ensemble of seven comprehensive atmosphere models. Using an ensemble of models forced with the same aerosol allows us to understand to what extent model differences unrelated to the aerosol lead to uncertainty in aerosol impacts on the circulation. This was not possible in previous studies that were based on a single model [Yoshimori and Broccoli, 2008; Allen and Sherwood, 2011; Ming and Ramaswamy, 2011; Ocko et al., 2014] or that employed different treatments of the aerosol across a model ensemble [Hwang et al., 2013; Allen et al., 2015].

Present understanding of how a localized heating affects the zonal-mean circulation and ITCZ position builds on the ideas of Kang et al. [2009]. In the annual and zonal mean, the ITCZ position (φ) is proportional to the cross-equatorial atmospheric energy transport (H), which itself is given by the hemispheric difference (Δ ; Northern minus Southern Hemisphere average) in atmospheric energy input by top-of-atmosphere shortwave (S) and longwave (L) radiative fluxes and the sum of surface radiative and turbulence fluxes (O),

$$\varphi = aH = \tilde{a}\Delta(S - L - O). \quad (1)$$

In equilibrium O is zero over land and balanced by ocean energy transport over the ocean. Equation (1) reflects the fact that an efficient way for the atmosphere to balance a hemispheric asymmetry in atmospheric energy input is to generate an anomalous cross-equatorial Hadley circulation that exports dry static energy from the heated into the cooled hemisphere in its upper level flow, and imports moisture in its low-level return flow. This implies that Northern Hemisphere heating by aerosol absorption should result in a northward ITCZ shift, while Northern Hemisphere cooling by aerosol scattering should result in a southward ITCZ shift [Yoshimori and Broccoli, 2008; Hwang et al., 2013; Allen et al., 2015].

Using equation (1) the ITCZ shift can be decomposed into a forced component $\delta\varphi^F$ that results from the aerosol-radiative forcing F , and a response component $\delta\varphi^R$ that results from the response R of the other top-of-atmosphere and surface fluxes to the aerosol forcing. That is,

$$\delta\varphi = \delta\varphi^F + \delta\varphi^R = \tilde{a}\Delta(F + R), \quad (2)$$

where the symbol δ indicates the aerosol-induced changes in the ITCZ position. This separates the aerosol impact into two subproblems. First, by subjecting models to the same aerosol perturbation we test to what extent model differences in F depend on radiative transfer, rapid adjustments, and the reference climate upon which the aerosol operates. Second, we test if model differences in $\delta\varphi$ arise mainly from model differences in F or R . These subproblems are helpful in determining the level of detail needed for aerosol processes in global climate models, in particular given the competition for computational capacities with other small-scale processes, e.g., those related to clouds.

The paper is organized as follows. The idealized aerosol, simulation protocol, and participating models are described in section 2. Section 3 characterizes the aerosol-radiative forcing across models. Section 4 analyzes the aerosol-induced ITCZ shifts. We separate fast and slow ITCZ shifts. The fast ITCZ shift results from the aerosol heating of the atmosphere and cooling of the land surface in the absence of sea-surface temperature (SST) changes. The slow ITCZ shift involves the aerosol impact on the ocean surface energy balance and is mediated by SST changes. Section 5 investigates to what extent model uncertainties in forcing

and response contribute to model uncertainty in ITCZ shifts. The paper closes with discussions and conclusions in section 6.

2. Idealized Anthropogenic Aerosol, Simulation Protocol, and Participating Models

2.1. The Idealized Aerosol

To ensure that the models see the same aerosol properties, we develop an analytic representation designed to capture the gravest mode of the anthropogenic aerosol's spatial variability. This facilitates the implementation of the aerosol in different models and also allows for an easy modification of the zonal distribution of the aerosol. We use the Max-Planck Institute Aerosol Climatology version 1 (MAC-v1) [Kinne *et al.*, 2013]. MAC-v1 provides an estimate of the current (year 2000) anthropogenic aerosol by combining AERONET ground-based remote sensing measurements and global models. The MAC-v1 anthropogenic aerosol and the idealization derived from it represent the net anthropogenic aerosol and include effects from both sulfate aerosol and black carbon. Figures 1a–1c show the annually averaged column aerosol optical depth (AOD) at a midvisible wavelength of 550 nm for the MAC-v1 anthropogenic aerosol.

We approximate the large-scale pattern of the anthropogenic aerosol by a superposition of Gaussian plumes in the zonal and meridional directions. The idealized aerosol is constant in time so that AOD at 550 nm is given by

$$\tau(x, y) = \tau_0 m(x) \cdot n(y). \quad (3)$$

m and n describe the zonal and meridional profile, respectively, x and y are deg longitude and deg latitude, and τ_0 is a scaling factor. In the meridional direction, the aerosol is modeled as a Gaussian plume centered at $y_0 = 35^\circ\text{N}$ and with a meridional width $\sigma_y = 25^\circ$ (Figure 1b, blue line),

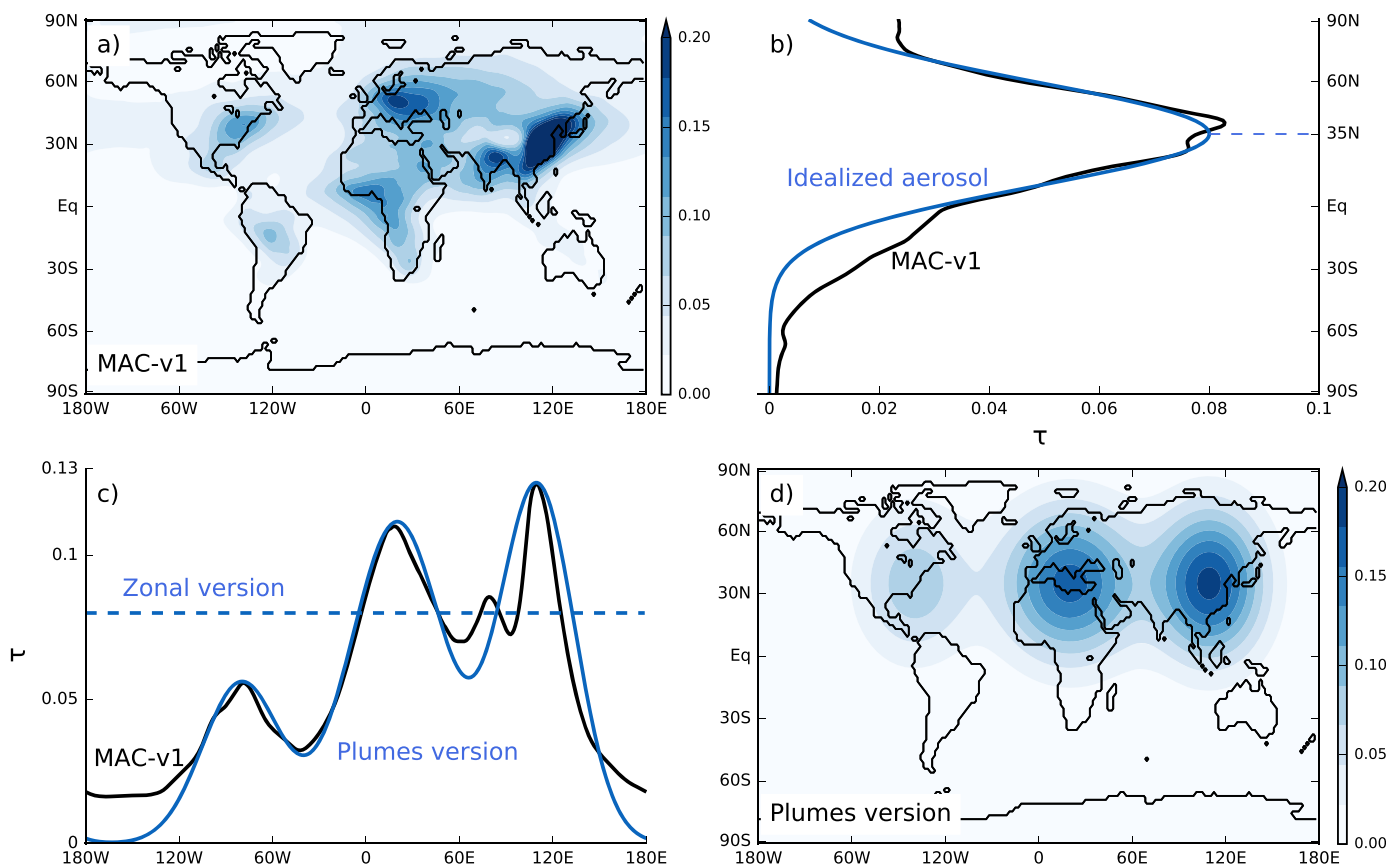


Figure 1. Column AOD at 550 nm of the anthropogenic aerosol and the idealized aerosol. (a) MAC-v1 climatology for the year 2000. (b) Zonally averaged meridional profile for MAC-v1 in black and the idealized aerosol in blue. (c) Meridionally averaged (between 10°S and 80°N) zonal profile (zonal version in dashed, plumes version in solid). (d) The plumes version of the idealized aerosol as a function of latitude and longitude.

Table 1. Parameters Defining the Latitude-Longitude Distribution of the Idealized Aerosol

AOD Scaling Factor	
τ_0	0.08 for zonal version 0.0932 for plumes version
Meridional Profile	
y_0	35°N
σ_y	25°
Zonal Distribution for Plumes Aerosol Version	
Europe	$x_1 = 20^\circ\text{E}; \sigma_{x,1} = 30^\circ; M_1 = 1.8$
Southeast Asia	$x_2 = 110^\circ\text{E}; \sigma_{x,2} = 24^\circ; M_2 = 2.0$
US	$x_3 = -80^\circ\text{E}; \sigma_{x,3} = 25^\circ; M_3 = 0.9$

$$n(y) = \exp\left(-\frac{(y-y_0)^2}{2\sigma_y^2}\right).$$

Two versions of the idealized aerosol are formulated that differ in the zonal distribution of the aerosol. The first is a zonally uniform version defined by $m(x) \equiv 1$. The second is a version that allows for zonal variation in aerosol loading. This is done to test if zonal variation in aerosol affects the ITCZ, for example by triggering stationary waves [Shaw et al., 2015] or due to different responses of the surface energy balances over land and ocean. The zonal variation is

described as the superposition of three Gaussian plumes in zonal direction centered over Europe/Africa ($i = 1$), Southeast Asia ($i = 2$), and the US/South America ($i = 3$) (Figure 1c, blue line),

$$m(x) = \sum_{i=1..3} M_i \exp\left(-\frac{(x-x_i)^2}{2\sigma_{x,i}^2}\right).$$

The centers x_i , widths $\sigma_{x,i}$, and magnitudes M_i of the zonal plumes are chosen such that the aerosol zonal distribution averaged between 10°S and 80°N approximates that of MAC-v1. The zonal distribution of the zonal and plumes version are depicted in Figure 1c; the longitude-latitude distribution of the plumes version is shown in Figure 1d. Fifty-five percent of the AOD is located over land for the plumes versions, compared to 38% for the zonal version. Table 1 provides a summary of the parameter values. To ensure that the global-mean AOD is the same in both versions, τ_0 is slightly larger in the plumes version. The global-mean column AOD at 550 nm is 0.033 for the idealized aerosol, compared to 0.037 in MAC-v1.

The vertical aerosol distribution is specified via the normalized extinction coefficient β in units of m^{-1} . Figure 2 shows the annual-mean β for MAC-v1 averaged between 10°S and 80°N and over all longitudes. This is approximated by a constant β from the local surface to $z_0 = 1250$ m, followed by an exponential decrease with height above z_0 ,

$$\beta = a \cdot \exp(-c \cdot z) \text{ for } z > z_0.$$

z is the local height above ground, and $a = 0.98657 \times 10^{-3} \text{ m}^{-1}$, $c = 0.75 \times 10^{-3} \text{ m}^{-1}$.

The spectral dependence of AOD is given by

$$\tau(\lambda) = \tau\left(\frac{\lambda[\text{nm}]}{550 \text{ nm}}\right)^{-\alpha}, \quad (4)$$

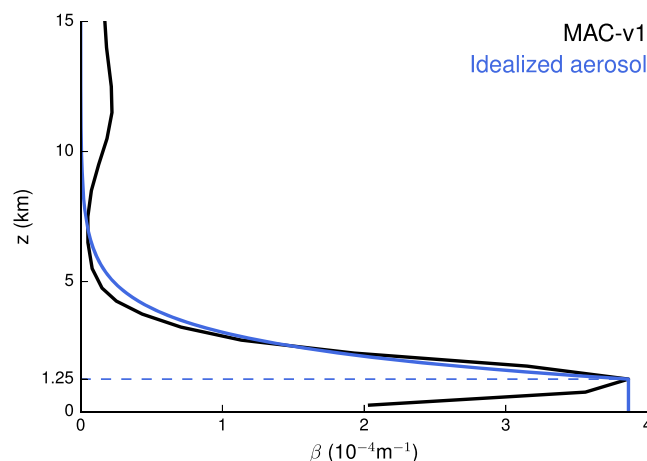


Figure 2. Vertical distribution of the idealized aerosol as defined by the normalized extinction coefficient, β , with respect to height above local ground, z . MAC-v1 is shown in black for comparison and has been averaged over all months, longitudes and between 80°N and 10°S.

where the Angstrom α exponent is set to $\alpha = 1.8$. The annually and zonally averaged single scattering albedo ω and asymmetry factor g vary only slightly with latitude in MAC-v1 and are set to spatially uniform values of $\omega = 0.926$ and $g = 0.65$. ω is obtained as the global-mean single scattering albedo at 550 nm from MAC-v1. g is biased low in MAC-v1 (S. Kinne, personal communication, 2014) and is thus set to a slightly higher value than what is derived from MAC-v1. ω and g do not depend on wavelength. The formulation of the idealized aerosol presented here could be readily modified to effect other patterns of aerosol absorption and scattering of radiation. As

such, it contributes to recent efforts to devise idealized aerosol formulations for global climate models to systematically study aerosol impacts on global and regional climate in large model ensembles [e.g., *Stevens et al., 2017; Toohey et al., 2016*]. Our formulation is more idealized, however, since the AOD horizontal distribution is simpler, the normalized vertical profile is the same at all longitudes and latitudes, and the aerosol is constant in time.

The aerosol is only active in the shortwave domain and is limited to aerosol-radiation interactions. Aerosol-cloud interactions and aerosol-snow ice interactions are omitted. With $\omega < 1$ the aerosol both scatters and absorbs shortwave radiation, thereby at the same time cooling the surface and heating the atmosphere. This introduces a tug-of-war on the ITCZ position, with aerosol scattering cooling the surface and leading to a southward ITCZ shift, and aerosol absorption heating the atmosphere and leading to a northward ITCZ shift.

Figure 3 and Table 2 characterize the aerosol instantaneous radiative forcing, I . I is derived from simulations with the ECHAM6 atmosphere model [*Stevens et al., 2013*] that are run for the years 1979–2008 and follow the Atmosphere Model Intercomparison Project (AMIP) setup [*Gates, 1992*]. SSTs, sea ice, ozone, solar insolation, and well-mixed greenhouse gases are prescribed to time-evolving observed values. I is diagnosed as the difference in shortwave irradiance between a radiation calculation that takes into account the aerosol, and a radiation calculation with zero aerosol. The model sees the radiative heating rates of the radiation calculation with the aerosol. We also calculated I with the ECHAM6-Tiedtke version of the ECHAM6 model that uses a different moist convection scheme [*Möbis and Stevens, 2012*] and found no impact on the zonal and global-mean I . The top-of-atmosphere (subscript t) instantaneous radiative forcing I_t is -1.1 in clear-sky and -0.6 W m^{-2} in all-sky conditions. This is within 0.1 W m^{-2} of what is derived for the anthropogenic aerosol in MAC-v1 [*Kinne et al., 2013*], and within the range given in *Boucher et al. [2013]*. When designing the idealized aerosol, we did not attempt to match the top-of-atmosphere forcing of the actual anthropogenic aerosol, but the close match is a welcome feature. The surface (subscript s) and atmospheric (subscript a) instantaneous radiative forcing are $I_s = -1.5$ and $I_a = 0.9 \text{ W m}^{-2}$. I_s and I_a are somewhat smaller in magnitude than what is estimated for the present-day anthropogenic aerosol from MAC-v1 and other studies [*Stier et al., 2013; Kinne et al., 2013*, and references therein]. They could be brought closer to observations by adapting the aerosol optical properties, and possibly its vertical distribution, but given the idealized nature of the aerosol such a fine-tuning is not explored here.

As expected from the spatial pattern of the aerosol, I predominates in the northern midlatitudes (Figure 3). The form of zonal distribution of the aerosol has little effect on zonal mean and global mean I (compare the zonal and plumes version in Table 2), indicating that surface albedo and background climate have little impact on I . The aerosol captures the positive I_t of the anthropogenic aerosol in the Arctic, where the high surface albedo reinforces the aerosol's absorbing effect [*Boucher et al., 2013*]. The hemispheric difference in I is about 50% larger than the global average (Table 2), creating ample potential for the aerosol to create a hemispheric contrast in atmospheric energy input and to shift the ITCZ. A fivefold increase in AOD leads to an about 5 times larger I .

2.2. Simulation Protocol and Participating Models

One aim of our paper is to separate the fast and slow aerosol impacts. The separation is motivated by the fact that the fast and slow impacts operate via thermal reservoirs of vastly different sizes, which leads to a difference in response time [*Sherwood et al., 2015*]. The fast impact operates via the energy balances of the small thermal reservoirs of the atmosphere, land, and sea ice. The fast impact thus is mainly driven by aerosol atmospheric heating, occurs in the absence of SST changes, and happens within a couple of weeks to months. In contrast, the slow impact operates via the large thermal reservoir of the ocean. The slow impact thus results from the impact of aerosol scattering on SSTs and requires a response of at least the upper ocean. This implies a timescale of around 10 years [*Woelfle et al., 2015*], with a possibly longer response time if the surface perturbation is mixed down to the deeper ocean.

To separate the fast and slow impacts, we apply the AMIP protocol of the Coupled Model Intercomparison Project Phase 5 (CMIP5) [*Taylor et al., 2012*], in which atmosphere-land components of Earth system models are driven with observed time-evolving SSTs, sea-ice cover, total solar irradiance, well-mixed greenhouse gases, ozone and land properties. The AMIP protocol has been applied successfully before to separate fast and slow CO_2 impacts [e.g., *Bony et al., 2013; Shaw and Voigt, 2015*]. The fast impact, sometimes also

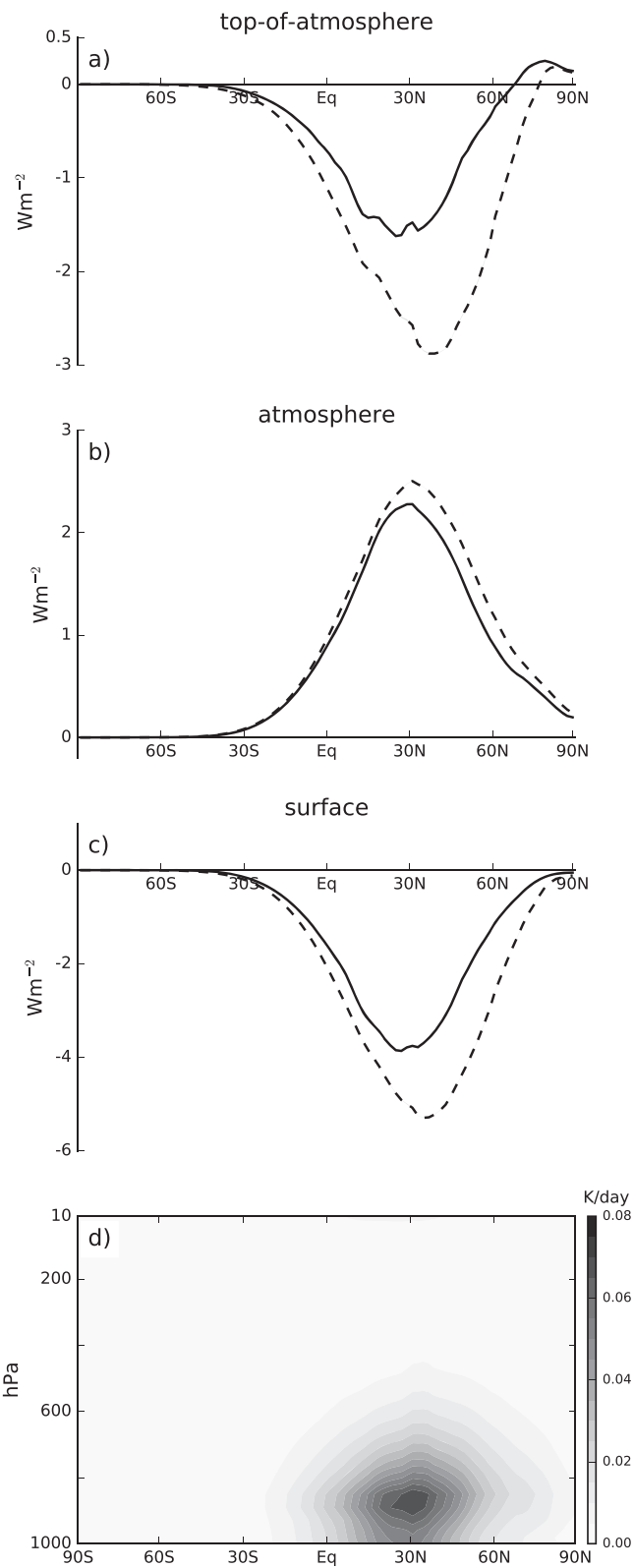


Figure 3. Annually and zonally averaged instantaneous radiative forcing of the idealized aerosol at (a) the top-of-atmosphere, (b) inside the atmosphere (top-of-atmosphere surface), and (c) at the surface. The all-sky forcing is shown in solid, the clear-sky forcing in dashed. Figure 3d shows the all-sky atmospheric radiative heating rate of the aerosol as a function of latitude and pressure. Pressure levels correspond to a surface pressure of 1000 hPa; in regions with topography the heating occurs at lower pressures because the aerosol's vertical distribution is defined with respect to the local height above ground. The plot shows the zonal version of the idealized aerosol; the same plot is obtained for the plumes version.

Table 2. Global and Hemispheric Instantaneous Radiative Forcing of the Aerosol Derived From a Double Radiation Call in the ECHAM6 Model^a

	Global Average			Hemispheric Difference (NH-SH)		
	Toa	Surface	Atmosphere	Toa	Surface	Atmosphere
ZONAL	-0.6 (-1.1)	-1.5 (-2.1)	0.9 (1.0)	-0.9 (-1.7)	-2.2 (-3.3)	1.4 (1.6)
PLUMES	-0.6 (-1.0)	-1.5 (-2.0)	0.9 (1.0)	-0.9 (-1.5)	-2.2 (-3.1)	1.4 (1.6)
ZONAL-5X	-2.5 (-4.7)	-7.0 (-9.5)	4.4 (4.8)	-3.4 (-6.9)	-10.3 (-14.4)	6.8 (7.5)
PLUMES-5X	-2.4 (-4.2)	-6.8 (-9.0)	4.4 (4.9)	-3.2 (-5.9)	-10.0 (-13.4)	6.9 (7.5)

^aThe ECHAM6-Tiedtke model gives the same result. Clear-sky values are in parentheses. All values are in units of $W m^{-2}$.

referred to as the response to direct radiative forcing, is obtained from simulations in which the idealized aerosol is introduced and SSTs are kept at the AMIP values. The slow impact, sometimes also referred to as the response to indirect SST changes, is obtained from simulations in which SSTs are changed.

Seven simulations are performed for each model. For all simulations the idealized aerosol is the only aerosol present in the atmosphere for radiative purposes. The control simulation CLEAN is free of any aerosol-radiative interactions. This is achieved by setting AOD to zero in the radiation calculation. The ZONAL and PLUMES simulations study the fast impact of the zonal and plumes aerosol versions, respectively. Two simulations called ZONAL-5X and PLUMES-5X are also performed. In these, AOD is increased by a factor of 5 to ensure that the aerosol forcing is large enough to drive a robust fast response. CLEAN, ZONAL, PLUMES, ZONAL-5X, and PLUMES-5X all use the AMIP SSTs. The slow impact is studied in two additional simulations in which SSTs are changed compared to the AMIP SSTs to include the aerosol impact on more slowly evolving SSTs. These simulations use the same aerosol as ZONAL and PLUMES, respectively, and are called ZONAL-DSST and PLUMES-DSST. The SST change is denoted by DSST ($D = \delta$). DSST was derived from slab-ocean simulations with the ECHAM6 model and varies from month-to-month but is independent of year. Its annual average is shown in Figure 4. DSST is limited to latitudes between 65°N and 30°S. This is done to prevent SSTs below freezing in the DSST simulations, which could lead to inconsistencies with the AMIP sea-ice fraction. It is also worth noting that the slow aerosol impact on precipitation and the ITCZ is estimated from the difference between CLEAN and ZONAL/PLUMES-DSST. This is justified because the fast impact will turn out to be much smaller than the slow impact.

Figure 5 shows that the ECHAM6 DSST simulations reproduce the aerosol-induced precipitation and ITCZ shifts of the ECHAM6 slab-ocean simulations. The DSST simulations thus successfully model the slow ITCZ shifts in response to a known SST change and set an upper bound on model robustness. All simulations are run from year 1979 to 2008. An exception is the CAM5 model, which is run from year 1979 to 2005. To remove initialization effects the year 1979 is not included in the analysis.

Seven models have performed the simulations (Table 3). Most models are either used in their CMIP5 version or include changes in preparation of CMIP6. An exception is the ECHAM6-Tiedtke model, which differs from

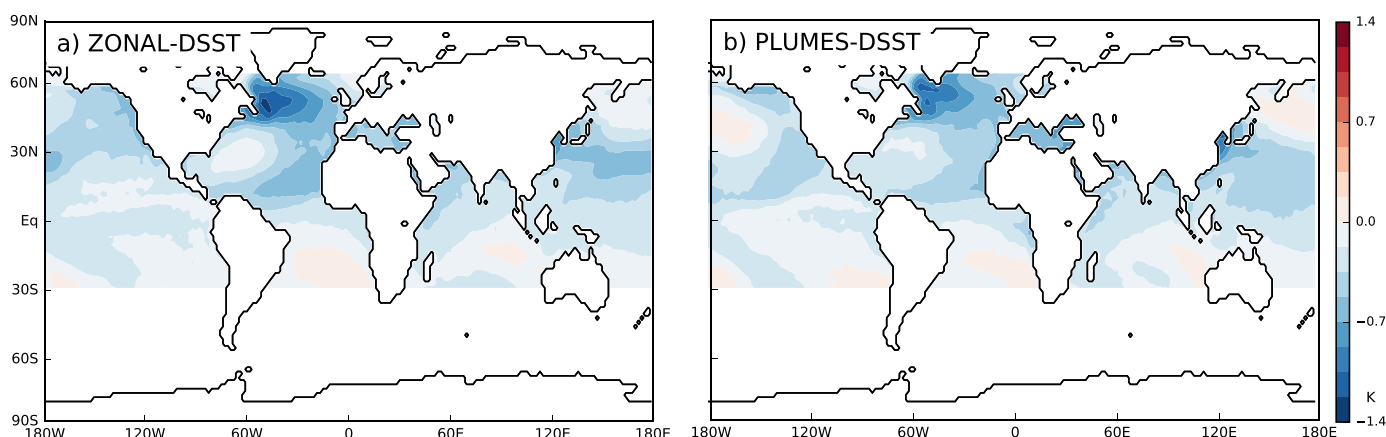


Figure 4. SST change (DSST) applied in the (a) ZONAL-DSST and (b) PLUMES-DSST simulations. DSST varies from month to month; here the annual-mean is shown.

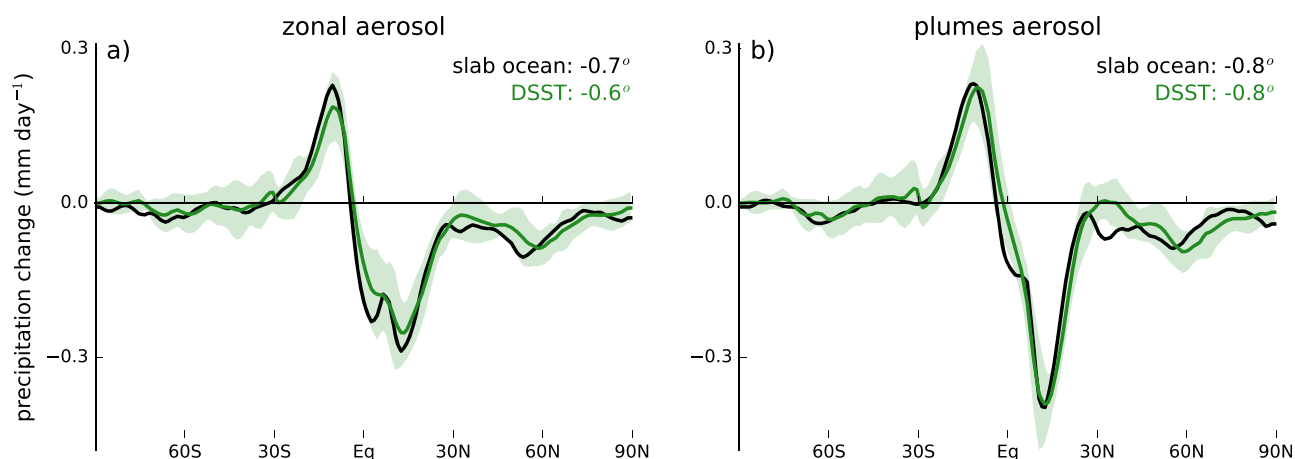


Figure 5. Annual and zonal-mean precipitation response in green for (a) the ZONAL-DSST and (b) the PLUMES-DSST simulations with the ECHAM6 model. The ECHAM6 slab-ocean simulations from which the DSST patterns were derived are shown in black for comparison. The numbers indicate the ITCZ shift in degree latitude, where the ITCZ position is calculated as the latitude of the precipitation centroid within 20°N/S. The green shading indicates the amount of internal variability in the DSST simulations that is estimated from the ECHAM6 five-member ensemble.

ECHAM6 in its treatment of moist convection. ECHAM6-Tiedtke has not been used for CMIP5 but is included here because moist convection had a substantial impact on the ITCZ in previous modeling studies [e.g., Möbis and Stevens, 2012; Voigt et al., 2014a, 2014b]. To estimate internal variability, ECHAM6 contributes five ensemble members for each simulations. As the aerosol impacts are calculated from the difference of the CLEAN simulation and an aerosol-containing simulation, this leads to $5 \times 5 = 25$ ECHAM6 estimates per aerosol and/or DSST perturbation. From these 25 estimates, we calculate internal variability as twice the standard deviation. For the CAM5 model, an error in the implementation of the plumes aerosol version was discovered after the simulations were completed, and so only CAM5 simulations with the zonal aerosol version are included in this paper.

3. Zonally and Globally Averaged Aerosol Radiative Forcing Across Models

Section 2.1 and Figure 3 characterized the aerosol based on the instantaneous radiative forcing in the ECHAM6 model. Recent research, however, has shifted attention to the effective radiative forcing that includes rapid atmosphere and land adjustments [Sherwood et al., 2015]. The adjustments occur independent of SST changes, and so the effective instead of the instantaneous forcing is relevant for slow aerosol impacts. For fast aerosol impacts the instantaneous forcing is more appropriate. Yet as we will show the aerosol atmospheric forcing that dominates the fast impact is not strongly affected by rapid adjustments and so the effective radiative forcing can also be used to understand fast ITCZ shifts. The effective forcing is given as the change in shortwave irradiance between the CLEAN simulation and the aerosol simulations

Table 3. List of Participating Models^a

	Model	Earth System Model	Reference	Remarks
1	ECHAM6	MPI-ESM	Stevens et al. [2013]	Five ensemble members per simulation
2	ECHAM6-Tiedtke	n/a	Möbis and Stevens [2012]	Tiedtke instead of Nordeng convection
3	CAM5	CESM1-CAM5	Neale et al. [2010] and Park et al. [2014]	Versions CAM5.3.42 and CESM1.3.beta11
4	BCC	BCC-CSM	Wu et al. [2010] and Zhang et al. [2014]	Version 2.0.1
5	HadGEM3-A	UKESM1 (CMIP6)	Hewitt et al. [2011]	Development version for CMIP6 successor of CMIP5 HADGem2-ES
6	CAM4	NorESM1-M/CCSM4	Neale et al. [2013] and Bentsen et al. [2013]	NorESM1-M expanded aerosol scheme and aerosol-cloud interactions are not used
7	LMDz5B	IPSL-CM5B	Hourdin et al. [2013]	

^aThe numbers in the first column are used in the plots to distinguish the models. All models except ECHAM6-Tiedtke are atmospheric components of Earth system models.

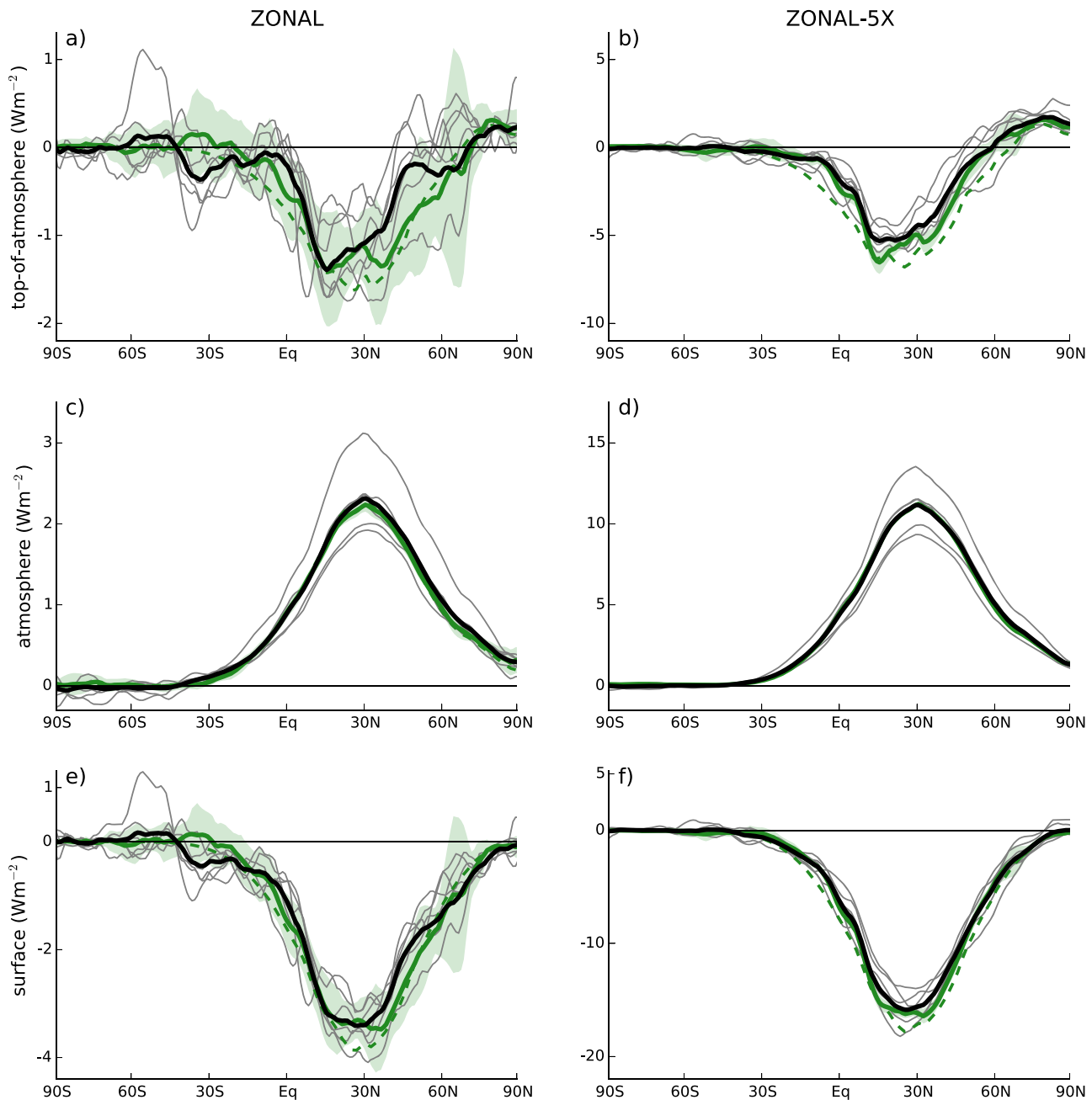


Figure 6. Annual-mean zonal-mean effective aerosol radiative forcing in the ZONAL (left) and ZONAL-5X (right) experiments at the top-of-atmosphere (a, b), inside the atmosphere (c, d) and at the surface (e, f). The thick black line is the multimodel mean; individual models are in gray. The thick green line is the ECHAM6 ensemble mean, and the green shading indicates the amount of internal variability. The green dashed line is the instantaneous aerosol radiative forcing diagnosed in the ECHAM6 model. Internal variability has no measurable impact on the instantaneous radiative forcing.

with AMIP SSTs (ZONAL, PLUMES, ZONAL-5X, and PLUMES-5X). While we will focus on the simulations with the zonal aerosol version in this section, we obtain the same results for the plumes version.

Figure 6 shows the effective forcing F for the ZONAL and ZONAL-5X simulations. The instantaneous forcing I is also included for ECHAM6 model. For the ECHAM6 model, F (solid green line) and I (dashed green line) show a very similar latitudinal variation, illustrating that rapid adjustments are small at individual latitudes. As for I , the latitudinal profile of F reflects the spatial distribution of the aerosol. Intermodel differences in the effective top-of-atmosphere forcing F_t and effective surface forcing F_s are indistinguishable from the

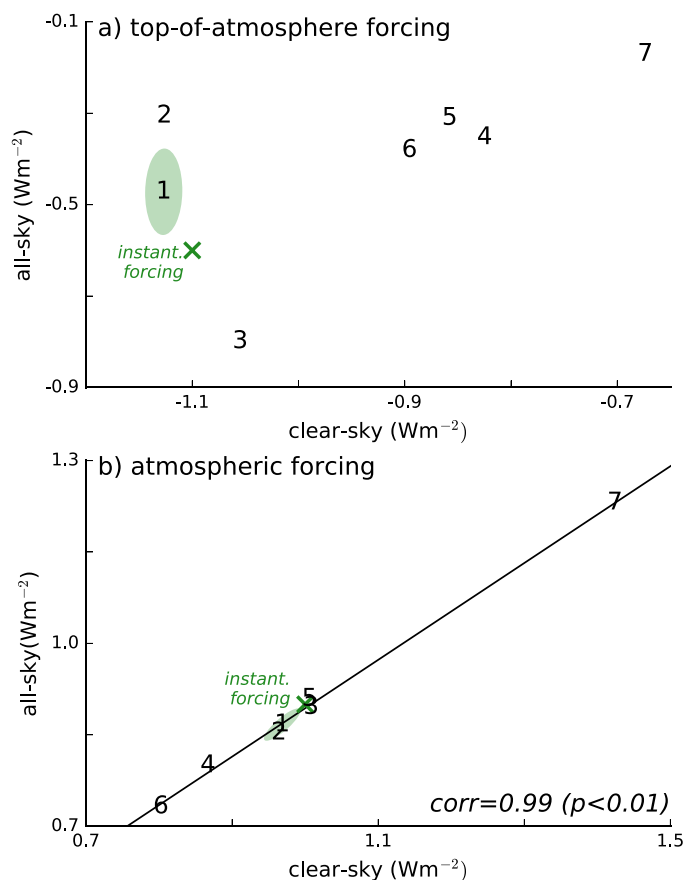


Figure 7. Model differences in the annual-mean global-mean (a) top-of-atmosphere and (b) atmospheric aerosol effective radiative forcing for all-sky versus clear-sky conditions. The numbers correspond to the model numbers in Table 3. The green x-mark is the instantaneous radiative forcing derived from the ECHAM6 and ECHAM6-Tiedtke models. The instantaneous radiative forcing closely agrees in the two models so that only one x-mark is visible. The green ellipse illustrates the magnitude of internal variability of the effective forcing derived from the ECHAM6 model. The plot shows the ZONAL simulation; the same result is obtained in the PLUMES simulation. Clouds have little impact on the atmospheric forcing but a large impact on the top-of-atmospheric forcing.

sphere average (with increased forcing magnitude). Globally averaged F_t and F_a differ by 50% or more of the multimodel mean between models in both clear-sky and all-sky conditions.

Model differences in aerosol forcing for the same aerosol perturbation are not unexpected [Boucher *et al.*, 1998; Randles *et al.*, 2013; Stier *et al.*, 2013]. In our simulations they arise predominantly from the underlying radiative transfer schemes and rapid cloud adjustments. This can be seen from the comparison of the ECHAM6 (model 1), ECHAM6-Tiedtke (model 2), and CAM5 (model 3), which use the same shortwave radiative transfer scheme (cf. Table A1), and the comparison of F and I in ECHAM6 and ECHAM6-Tiedtke. All-sky F_t differs substantially between the three models. This is mainly a result of model-dependent rapid cloud adjustments. Radiative transfer schemes also appear to play a role for differences across the entire model ensemble, as can be seen from the model differences in clear-sky F_t . Model differences in F_a , in contrast, are not affected by cloud adjustments but are essentially entirely driven by differences among the radiative transfer schemes. Further analysis indicates, however, that they are not the result of model differences in the number of shortwave spectral bands, as has been implicated for water-vapor shortwave absorption [DeAngelis *et al.*, 2015], or from how the band-averaged aerosol-optical depth is implemented (see Appendix A). While more work is needed to identify the reasons for radiation scheme-induced model differences in aerosol forcing [Pincus *et al.*, 2016], the next sections assess how the aerosol forcing underlying the aerosol's fast and slow impacts affect the ITCZ and to what extent model differences in aerosol forcing identified here explain model differences in ITCZ shifts.

internal variability of the ECHAM6 ensemble (green shading in Figure 6) for the realistic aerosol loading used in ZONAL, with internal variability being quite substantial at individual latitudes because of clouds. The multimodel mean closely agrees with the ECHAM6 ensemble mean. Intermodel differences in top-of-atmosphere and surface forcing become apparent only when AOD is increased to an unrealistically large value in the ZONAL-5X simulation.

Intermodel differences in absorption are striking. Cloud internal variability has little impact on the effective atmospheric forcing F_a and intermodel differences exceed the variability in the ECHAM6 ensemble even for the ZONAL simulation, with differences in peak absorption as large as 1 W m^{-2} (50% of the multimodel mean). Therefore, even though models see the exact same aerosol, they strongly differ in the aerosol forcing inside the atmosphere.

Figure 7 shows F_t and F_a at the global scale. Taking the global average reduces the impact of cloud internal variability, which helps to identify model differences in F_t . To ease comparison with previous studies, we focus on the global average, but the same results are obtained for the Northern Hemisphere

4. Fast and Slow Aerosol Impacts on Zonal-Mean Precipitation and ITCZ Position

The response of annual-mean zonal-mean precipitation is shown in Figure 8. The fast precipitation response in the ZONAL and PLUMES simulations is small and mostly indistinguishable from internal variability (Figures 8a and 8b). A clear fast response emerges only when AOD is increased to unrealistically high values in the 5X simulations (Figures 8c and 8d). In that case, precipitation decreases near the center of the aerosol plume around 30°N and in the Southern tropics, and shows little change in the Northern tropics.

This pattern results from the superposition of a local evaporation decrease and a meridional shift in moisture convergence. The local evaporation decrease is shown by the blue dashed line in Figures 8c and 8d. It peaks near 30°N and roughly follows the latitudinal distribution of the aerosol atmospheric heating. The

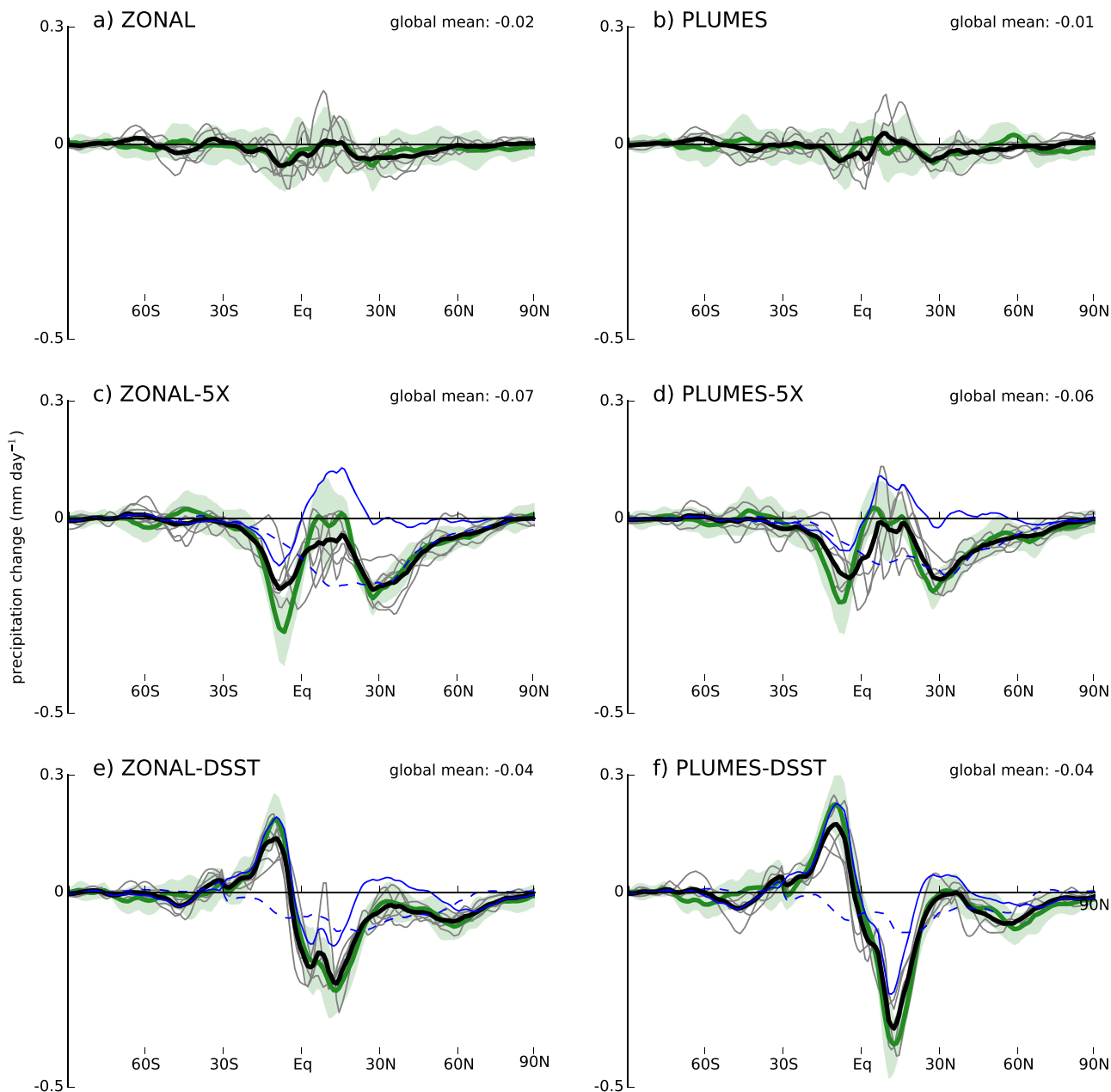


Figure 8. Response of annual-mean zonal-mean precipitation to the idealized aerosol. The thick black line is the multimodel mean. Individual models are in gray. The ensemble-mean of the ECHAM6 model is shown by the green line. The magnitude of internal variability estimated from the ECHAM6 model is shown by the green shading. For Figures 8c–8f, the multimodel mean change in evaporation and precipitation–evaporation are shown by the thin blue dashed and solid lines. The global-mean multimodel mean precipitation change is given in the top-right corners.

aerosol atmospheric heating compensates for some of the radiative cooling of the atmosphere, which decreases the need for warming by water-vapor condensation and hence precipitation. This mechanism was reported before for global-mean precipitation [Allen and Ingram, 2002; Andrews et al., 2010; Fläschner et al., 2016]; here we find that it also constrains surface evaporation at individual latitudes. One can also understand the reduced evaporation as the result of aerosol atmospheric heating and the decrease in the temperature contrast between the ocean surface and the near-surface atmosphere (recall that SSTs are fixed).

The shift in moisture convergence, which is measured by the change in precipitation minus evaporation, is shown by the blue solid line in Figures 8c and 8d. It signals anomalous advection of moisture from the Southern into the Northern hemisphere that arises from a northward shift of the ITCZ and an anomalous clockwise Hadley circulation. The circulation change is consistent with the aerosol warming of the Northern Hemisphere atmosphere as a whole relative to the Southern Hemisphere, because this forces a hemispheric difference in the atmospheric energy budget and southward cross-equatorial energy transport. In the Northern tropics the local evaporation decrease and the ITCZ shift nearly cancel each other, leading to an overall small precipitation change. For the slow response studied in the DSST simulations, the precipitation change is dominated by the circulation-induced change in moisture convergence and the associated southward ITCZ shift. The southward ITCZ shift is expected from the Northern Hemisphere cooling of the ocean surface (Figures 8e and 8f).

Figure 9 shows that the precipitation response and ITCZ shift are not zonally uniform. Most of the fast precipitation response originates from the Asian sector (Figures 9c and 9d). The zonal structure in the precipitation suggests a considerable impact of aerosol on monsoonal circulations [Meehl et al., 2008; Bollasina et al., 2011], motivating future applications of idealized aerosol perturbations. However, the slow SST-mediated precipitation response is much more uniform in longitude than the fast response that occurs in the absence of SST changes. This indicates that SST coupling reduces the impact of the zonal aerosol distribution on the regional precipitation response.

The ITCZ shifts are more formally quantified in Figure 10, where they are calculated as the latitude of the precipitation centroid within 20°N/S (same area-integrated annual-mean precipitation north and south of the ITCZ) [e.g., Frierson and Hwang, 2012]. Following equation (1) the ITCZ shifts are plotted as a function of the anomalous cross-equatorial energy transport by the atmosphere. The figure shows the expected negative correlation between the ITCZ shift and energy transport, as well as the expected tug-of-war between the northward fast ITCZ shift and the southward slow ITCZ shift. Fast and slow ITCZ shifts roughly fall on the same line.

This indicates that different from some other studies [Hill et al., 2015; Seo et al., 2017], total gross moist stability, i.e., the total moist static energy transport per unit mass transport, remains constant near the equator in our simulations. Consistent with this, the ITCZ transport ratio is not statistically different between the zonal and plumes versions of the aerosol. The ratio is twice as large as what was found by Donohoe et al. [2013] and for simulations of global warming and paleoclimates. The quantitative difference invites future research on factors that set the ITCZ-transport ratio, but this direction is not further investigated here.

The fast and slow ITCZ shifts are very different in magnitude. Across all models the fast ITCZ shift is much smaller than the slow ITCZ shift. In fact, even when the aerosol loading is strongly increased in the 5X simulations, the fast ITCZ shift is still smaller than the slow ITCZ shift in response to a realistic aerosol magnitude. To understand why this is the case, Figure 11 shows the ITCZ shifts as a function of the hemispheric difference in the underlying aerosol forcing, ΔF . The underlying aerosol forcing is different for the fast and slow ITCZ shifts. For the fast ITCZ shift, SSTs are fixed to the CLEAN control values while land and sea-ice temperatures are interactive. The relevant forcing is therefore the sum of the aerosol atmospheric forcing over ocean and the aerosol top-of-atmosphere forcing over land and sea ice. That is,

$$\Delta F^{\text{fast}} = \Delta(f \cdot F_t + (1-f) \cdot F_a), \quad (5)$$

where f is the fraction of a grid box covered by land or sea ice. Because F_a is larger than F_t (in absolute terms), $\Delta F^{\text{fast}} > 0$ and the ITCZ shifts northward. For the slow ITCZ shift, the forcing includes an additional term X that represents the SST change,

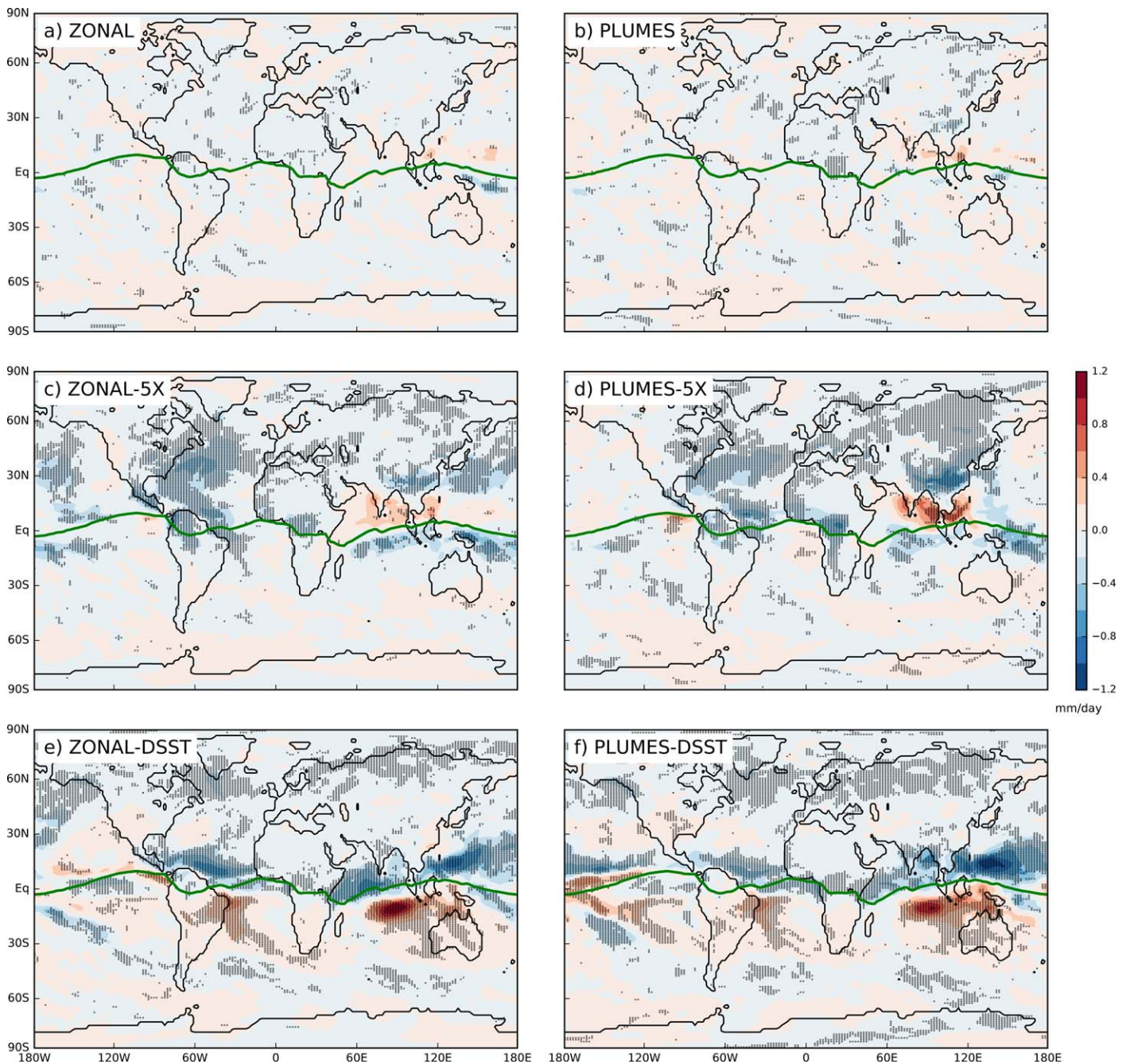


Figure 9. Multimodel mean response of annual-mean precipitation to the idealized aerosol. The green line is the multimodel mean ITCZ position in CLEAN. Regions in which all but one model agree on the sign of the response are stippled.

$$\Delta F^{\text{slow}} = \Delta F^{\text{fast}} + X. \quad (6)$$

To obtain X , we use that the DSST pattern was derived from ECHAM6 slab-ocean simulations, for which the relevant forcing is the aerosol top-of-atmosphere forcing from the ECHAM6 ZONAL and PLUMES simulations. Therefore,

$$\Delta F^{\text{slow,ECHAM6}} = \Delta F_t^{\text{ECHAM6}}$$

This allows us to calculate X from the ECHAM6 model using equations (5) and (6). X is the same in all models, and so model differences in ΔF^{slow} result entirely from model differences in ΔF^{fast} . X and ΔF^{slow} are smaller than 0, consistent with the slow ITCZ shift being southward.

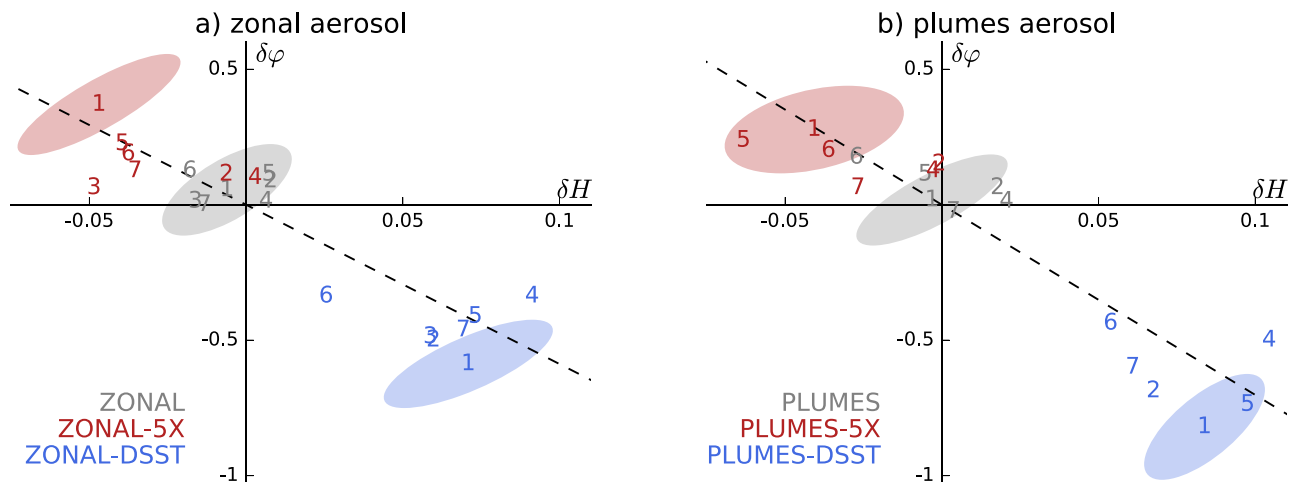


Figure 10. ITCZ shift $\delta\varphi$ (y axis; units of deg lat) as a function of the change in cross-equatorial energy transport δH (x axis; units of PW) in simulations with (a) the zonal aerosol and (b) the plumes aerosol. The dashed lines are linear regressions through all models and simulations; the slope is $-(5.9 \pm 0.6)$ deg lat/PW for the zonal aerosol and $-(7.0 \pm 0.7)$ deg lat/PW for the plumes aerosol. This indicates that the ratio between ITCZ shift and energy transport is insensitive to the spatial distribution of the aerosol. The numbers correspond to the model numbers in Table 3. The shaded ellipses indicate the internal variability estimated by the ECHAM6 model (model 1).

In contrast to the ITCZ-transport ratio, the ITCZ-forcing ratio differs markedly between the slow and fast ITCZ shifts (Figure 11). The ratio is 10 times larger for the slow ITCZ shift than the fast ITCZ shift. This is robust across all models. Thus, the same 1 W m^{-2} of aerosol forcing has a much larger impact on the ITCZ position when applied as a cooling of the ocean surface than when applied as a heating of the atmosphere and a cooling of the land surface.

The stark contrast in the ITCZ-forcing ratio arises from different responses of the atmospheric energy input. The response of the atmospheric energy budget for the fast ITCZ shift is analyzed in Figure 12a. The figure shows the model-mean aerosol forcing, the response of the other atmospheric energy budget terms, and the response of the net atmospheric energy input for the ZONAL-5X simulation. Most of the aerosol forcing is compensated locally, because of which the net atmospheric energy input and cross-equatorial energy transport only change little. The local compensation of the aerosol forcing implies that the fast ITCZ shift is small. The local compensation is realized mostly as a decrease in evaporation over ocean, supported by a smaller decrease in surface sensible heat flux and a reduced atmospheric energy loss by emission of long-wave radiation. All three changes are consistent with the aerosol-induced increase in atmospheric

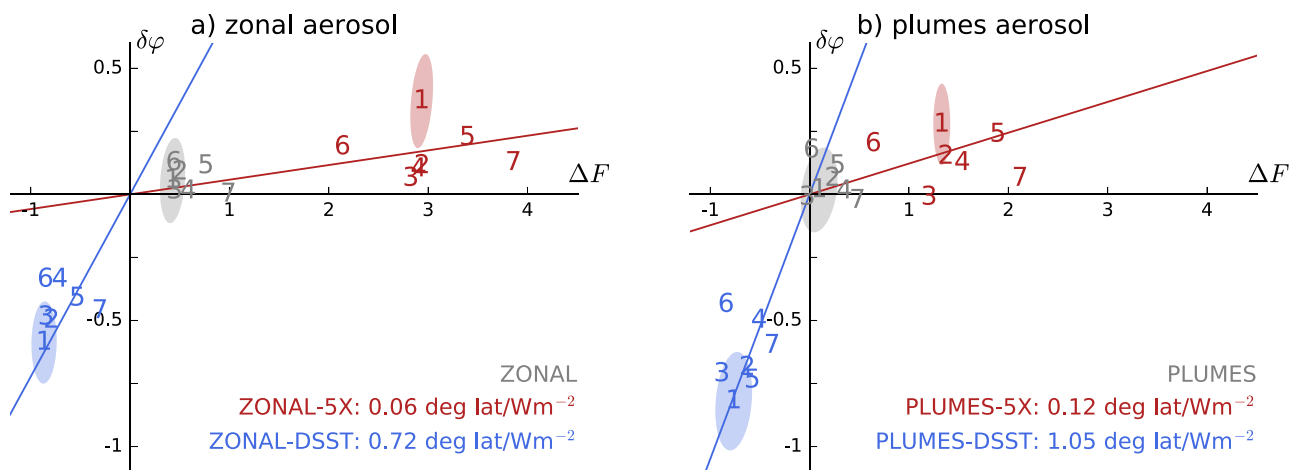


Figure 11. ITCZ shift $\delta\varphi$ (y axis; units of deg lat) in response to (a) the zonal and (b) the plumes aerosol as a function of the underlying aerosol radiative forcings ΔF^{fast} and ΔF^{slow} (x axis; units of W m^{-2}). The lines are linear regressions through zero. The values in the lower-right corner indicate the ITCZ-forcing ratio, i.e., the ITCZ shift that results from a 1 W m^{-2} hemispheric difference in aerosol forcing. The numbers correspond to the model numbers in Table 3. The shaded ellipses indicate the internal variability estimated from the ECHAM6 model (model 1).

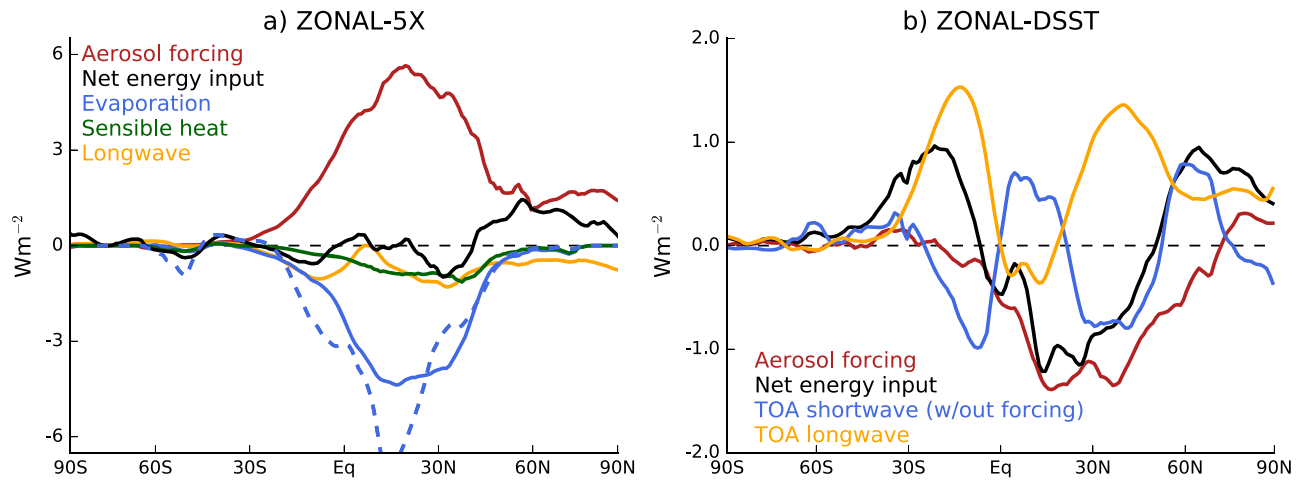


Figure 12. Equilibration of the atmosphere energy budget to the aerosol forcing for (a) the fast ITCZ shift simulated in the ZONAL-5X simulation and (b) the slow ITCZ shift simulated in the ZONAL-DSST simulation. Positive values correspond to heating of the atmosphere and imply a northward ITCZ shift if they occur in the Northern Hemisphere, and a southward ITCZ shift if they occur in the Southern Hemisphere. For Figure 12a model-mean values are shown. The dashed blue line shows the decrease in surface evaporation predicted by the increase in near-surface air temperature over fixed SSTs according to equation (8) where a near-surface relative humidity of 80% is assumed. Figure 12b shows the ECHAM6 model from which the DSST pattern was derived through slab-ocean simulations. TOA changes in the ECHAM6 DSST simulation closely trace those of the ECHAM6 slab-ocean simulation (cf. Figure 13).

temperatures over fixed SSTs. Indeed, the decrease in evaporation approximately scales with the local increase in near-surface air temperature, as is shown by the dashed blue line in Figure 12a. The scaling is derived by linearizing the equation for surface evaporation E ,

$$E = C \{q_{sat}(T_s) - r q_{sat}(T)\}, \quad (7)$$

around the local fixed surface temperature T_s and assuming that aerosol-induced changes in the transfer coefficient C and near-surface relative humidity r are small. q_{sat} is the saturation specific humidity, and T is the surface air temperature. With this, the evaporation decrease scales approximately as

$$\delta E \simeq -r \delta T \frac{E}{T_s - T}, \quad (8)$$

where E , T , and T_s are taken from the CLEAN simulation.

For the slow ITCZ shift studied by the DSST simulations, the surface energy balance is approximately closed and the underlying aerosol forcing is the aerosol top-of-atmosphere forcing over both ocean and land/sea-ice areas. Changes in atmospheric energy input can thus be deduced from the top-of-atmosphere energy balance. Figure 12b shows the change in the top-of-atmosphere energy balance for the ZONAL-DSST simulation with the ECHAM6 model. The energy balance change is decomposed into the aerosol forcing (equation (6)), changes in outgoing longwave radiation, and additional changes in shortwave radiation that result, for example, from cloud and water-vapor changes coupled to the ITCZ shift [e.g., Voigt *et al.*, 2014a; Yoshimori and Broccoli, 2009]. Although the longwave and additional shortwave changes are substantial, they largely cancel each other, and the change in net atmospheric energy input is close to the aerosol forcing. In contrast to the fast ITCZ shift, the aerosol forcing is thus not locally compensated and readily affects the net atmospheric energy input. As a result, when normalized with respect to the underlying aerosol forcing the slow ITCZ shift is an order of magnitude larger than the fast ITCZ shift.

5. Model Robustness in Fast and Slow ITCZ Shifts

In this section we shift attention to the question of model robustness in aerosol-induced ITCZ shifts. To this end we assess to what extent the ITCZ shifts differ between models, and if these differences are linked to model differences in aerosol forcing. We again use Figure 11 and separately analyze fast and slow ITCZ shifts.

5.1. Fast ITCZ Shift

When models are perturbed with a realistic aerosol loading (ZONAL and PLUMES simulations), the fast ITCZ shift is so small that it prevents a meaningful analysis of model differences. We therefore focus on the 5X simulations, in which the fast ITCZ shift differs by about 0.4° across models. While this is larger than internal variability, it is of little practical relevance and so models overall show good agreement on the fast ITCZ shift. Models differ quite strongly, however, in the hemispheric difference in aerosol forcing that underlies the fast ITCZ shift. The hemispheric forcing difference between the model with the smallest forcing (CAM4) and the model with largest forcing (LMDz5B) is 1.7 W m^{-2} for the zonal aerosol and 1.5 W m^{-2} for the plumes aerosol. Despite the large forcing difference, however, the two models predict very similar ITCZ shifts that are close to the multimodel mean. Aerosol forcing agrees within 0.1 W m^{-2} in the ECHAM6, ECHAM6-Tiedtke, CAM5 and BCC models, yet the ITCZ shift differs much more between these four models than between the CAM4 and LMDz5B models. Thus, aerosol forcing is a poor predictor of the fast ITCZ shift, and any model differences in the fast ITCZ shift, as small as they may be, cannot be attributed to model differences in aerosol forcing.

5.2. Slow ITCZ Shift

As for the fast ITCZ shift, model differences in the slow ITCZ shift obtained from the DSST simulations are limited to a few tenths of a degree. Thus, models show good agreement in the response of the ITCZ to a given SST perturbation. This is not only true in the zonal mean but also at many individual longitudes, as can be seen from Figures 9e and 9f. As for the fast ITCZ shift, there is no relation between model differences in the ITCZ shift and the underlying aerosol forcing. This is not surprising, however, because model differences in the forcing plotted in Figure 11 are purely due to model differences in the forcing that underlies the fast ITCZ shift (recall that X of equation (6) is the same in all models).

The good agreement across models when perturbed with the same SST pattern is in some contrast to previous studies that reported large model differences in ITCZ shifts reaching up to several degrees latitude [Kang *et al.*, 2008; Voigt *et al.*, 2014a]. In these studies SSTs were interactive, which raises the question whether models would differ more if they were allowed to predict their own SSTs. A full answer to this question requires simulations with interactive SSTs. Nevertheless, we can obtain a partial answer from the DSST simulations.

The ECHAM6 model provides both prescribed and interactive-SST simulations. Comparing the ECHAM6 DSST and slab-ocean simulations, we find that the prescribed-SST setup successfully reproduces not only the aerosol-induced precipitation change and ITCZ shift of the interactive-SST setup (Figure 5), but also the change in the TOA energy balance (Figure 13). Figure 13 also shows the TOA change for all models. There is substantial model spread in the TOA change that at some latitudes is as large as the change in ECHAM6. In the prescribed-SST setup the model differences in the TOA change have little impact on the ITCZ since they are mostly compensated by similar model differences in the surface energy balance change. For interactive-

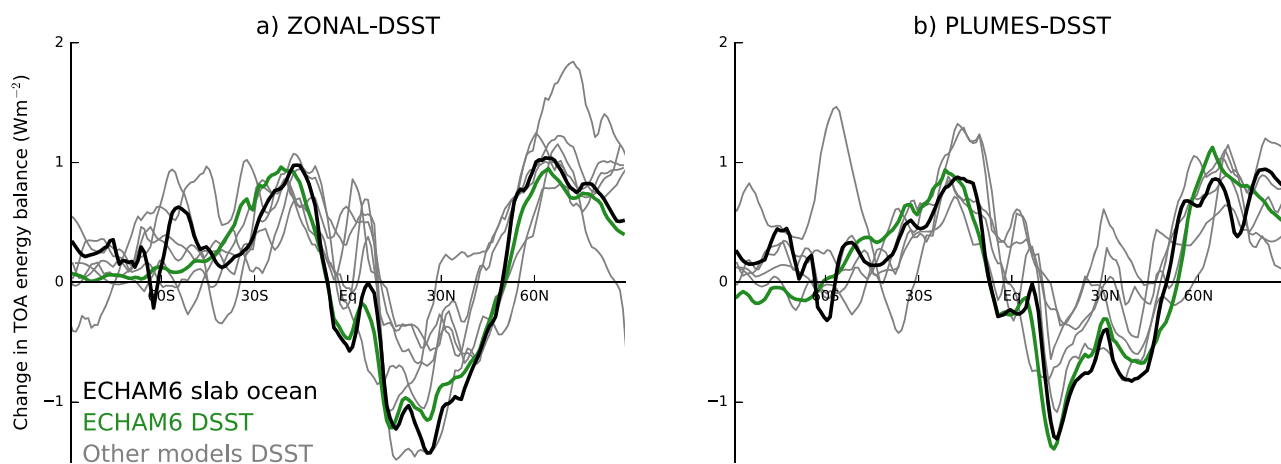


Figure 13. Response of the time-mean zonal-mean TOA energy balance in the DSST simulations with respect to the CLEAN simulation for (a) the zonal aerosol and (b) the plumes aerosol. The ECHAM6 model is highlighted in green, and the change simulated in the ECHAM6 slab ocean setup is shown in black for comparison.

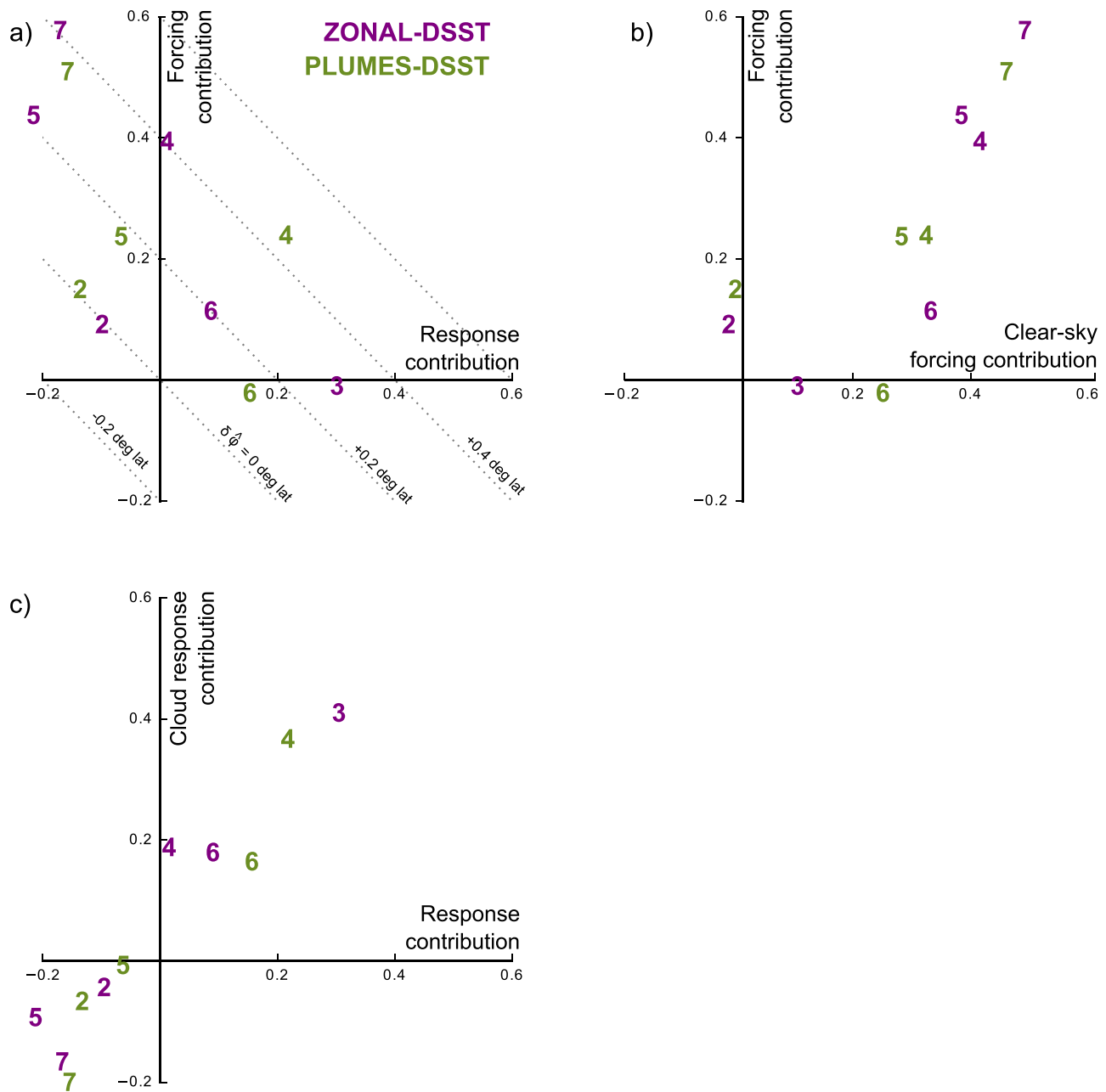


Figure 14. Estimate of the additional ITCZ shift $\delta\hat{\varphi}$ that would occur if models were coupled to an interactive-SST surface. The additional ITCZ shift is expressed relative to the ECHAM6 model (model 1), which is thus not included in the plot. (a) The magnitude of $\delta\hat{\varphi}$ can be read from the slanted dashed lines. $\delta\hat{\varphi}$ is decomposed into a contribution from model differences in top-of-atmosphere aerosol radiative forcing (y axis) and a contribution from model differences in the TOA response (x axis). (b) The contribution from model differences in aerosol forcing versus model differences in clear-sky aerosol forcing. (c) The contribution from model differences in the TOA response versus model differences in the change of cloud-radiative effects. All energetic quantities are converted into ITCZ shift units (deg latitude) using the scaling of 6.5 deg lat/PW from Figure 10.

SSTs, however, the surface energy balance change would be zero, and the TOA model differences would trigger an ITCZ shift $\delta\hat{\varphi}$ that is in addition to the slow ITCZ shift $\delta\varphi$ simulated in the DSST simulation.

We therefore use the TOA change to estimate the additional ITCZ shift $\delta\hat{\varphi}$. This allows us to estimate how the use of interactive instead of prescribed SSTs would affect model differences in the slow ITCZ shift. For each model we calculate the difference of its TOA change from ECHAM6 and convert this difference to $\delta\hat{\varphi}$ using the 6.5°/PW scaling derived in Figure 10 (average of zonal and plumes aerosol versions). The model differences in the TOA change relative to ECHAM6 translate to $\delta\hat{\varphi}$ values from 0° to 0.4° as can be read from the dashed lines in Figure 14a. $\delta\hat{\varphi}$ in some models is as large as the model spread of the ITCZ shift of

the DSST simulations. This indicates that the model spread in the slow ITCZ shift would double if SST were interactive.

We further diagnose what processes lead to $\delta\hat{\varphi}$. To this end we use equation (2) and decompose $\delta\hat{\varphi}$ into a contribution related to model differences in aerosol forcing, and a contribution related to model differences in how the TOA energy balance responds to the aerosol via, e.g., changes in clouds. The forcing contribution arises from the difference of the all-sky top-of-atmosphere aerosol forcing between a model and ECHAM6. The response contribution is the residual between $\delta\hat{\varphi}$ and the forcing contribution. Figure 14a shows that both the forcing and response contributions vary by 0.5° across models.

For the forcing contribution, Figure 14b shows that much of the model differences result from the clear-sky forcing. Thus, while model differences in radiative transfer schemes are not strongly felt in a prescribed-SST setup, they are expected to cause substantial model differences in ITCZ shifts in interactive-SST setups. This highlights that an accurate treatment of radiative transfer is necessary, albeit not sufficient, to obtain reliable model estimates of ITCZ shifts in particular, and of the circulation and climate responses to radiative forcings in general [Pincus *et al.*, 2016].

Figure 14c shows that the response contribution is closely related to model-dependent changes in cloud-radiative effects. This indicates that cloud-radiative changes, whose shortwave component is largely felt at the surface and which thus do not impact the ITCZ when SSTs are prescribed, would lead to substantial model differences in ITCZ shifts when SSTs were interactive. Model spread in the cloud response is not robustly tied to a particular region or cloud regime across models, however.

6. Implications for Aerosol Representation in Global Climate Models and Attribution of Past Precipitation Changes

In this paper we develop an idealization of the anthropogenic aerosol to test fast and slow aerosol impacts on the position of the zonal-mean tropical rain belt, i.e., the intertropical convergence zone (ITCZ). To this end we run seven comprehensive atmosphere models with prescribed sea-surface temperatures (SST). The fast impact occurs in the absence of SST changes and is caused by the aerosol heating of the atmosphere and cooling of the land surface. The slow impact is mediated by SST changes. We implement two versions of the aerosol that differ in the zonal distribution of the aerosol, but this is found to have little impact on the zonal-mean ITCZ shift.

We find that the fast and slow ITCZ shifts oppose each other (northward fast shift, southward slow shift) and that the slow ITCZ shift dominates over the fast ITCZ shift. This is consistent with previous work [e.g., Yoshimori and Broccoli, 2008; Allen and Sherwood, 2011; Ocko *et al.*, 2014]. We also present an in-depth analysis of the atmospheric energy budget that shows that the tug-of-war between fast and slow ITCZ shifts is a result of opposite aerosol forcings (heating of Northern Hemisphere atmosphere by aerosol absorption versus cooling of Northern Hemisphere ocean surface). More importantly, however, we demonstrate that for the same unit of aerosol forcing the slow ITCZ shift is 10 times stronger than the fast ITCZ shift. This result is robust across models and arises because the atmospheric heating by aerosol absorption is largely compensated by a local decrease of surface evaporation over the ocean.

The small fast ITCZ shift implies that model differences in aerosol atmospheric forcing, which are substantial in our model ensemble due to the underlying radiative transfer schemes, are unimportant for model differences in zonal-mean ITCZ shifts. This is independent of the timescale and true for both the fast and slow responses. Models agree well on the slow response when perturbed with the same SST change. Yet, there are reasons to believe that the slow response would be much more different across models if models were predicting their own SST response. The first source of likely increased model differences in interactive-SST setups are differences in clear-sky top-of-atmosphere forcing that arise from differences in clear-sky radiative transfer schemes. However, as radiation schemes are being updated [Pincus *et al.*, 2015], model differences in aerosol forcing should play a smaller role in future studies. The second source is model-dependent rapid cloud adjustments and the response of clouds to the aerosol-induced SST change. Clouds thus represent the arguably most important and most challenging obstacle for quantitative model estimates of ITCZ shifts [Kang *et al.*, 2008; Frierson and Hwang, 2012; Voigt *et al.*, 2013, 2014b]. In contrast, the fact that the zonal and plumes version of the idealized aerosol yield similar zonal-mean ITCZ shifts and that SST coupling

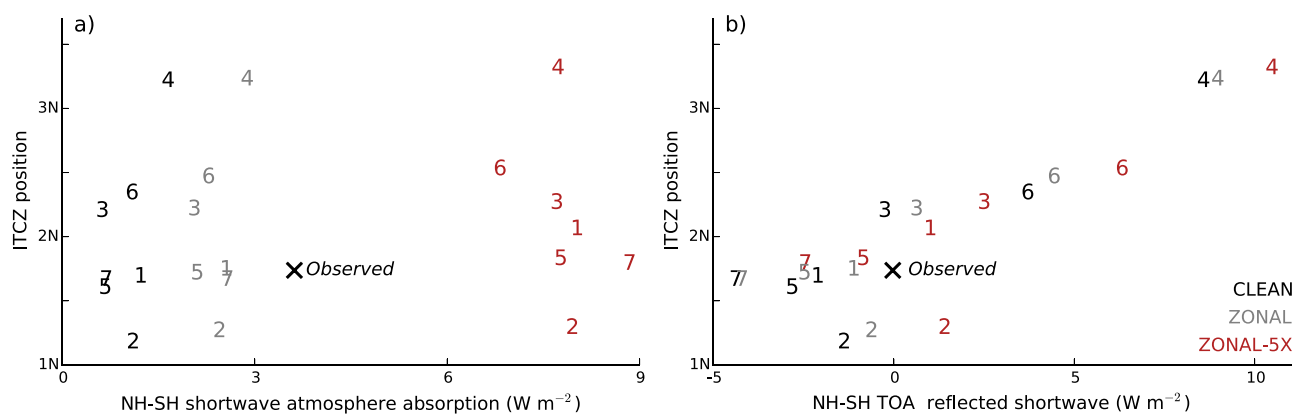


Figure 15. (a) ITCZ position as a function of the hemispheric difference in atmospheric shortwave absorption (Northern minus Southern Hemisphere) in the CLEAN (black), ZONAL (gray), and ZONAL-5X (red) simulations. (b) Same as in Figure 15a but for hemispheric difference in top-of-atmosphere shortwave reflection. The cross shows observed radiative fluxes from the CERES EBAF-TOA and SFC [Loeb et al., 2009; Kato et al., 2013] edition 2.8 averaged over years 2000–2016, and observed ITCZ position derived from GPCP v2.2 precipitation [Adler et al., 2003] averaged over years 1981–2010.

makes the tropical precipitation response more zonally uniform indicates that knowledge of the aerosol radiative forcing on the hemispheric scale is sufficient.

The good model agreement on the ITCZ shift in response to a given SST change shows that the aerosol impact on zonal-mean tropical rainfall is, from a practical point of view, incorporated in the impact of aerosol on SSTs. For recent observed climates for which SSTs are known with good accuracy, this has two implications. The first is that model deficiencies in the simulation of the present-day ITCZ cannot be attributed to the representation of aerosol when SSTs are prescribed to observed values.

This is illustrated in Figure 15a, which shows that the ITCZ position in a prescribed-SST setup is insensitive to aerosol atmospheric shortwave absorption. Unless aerosol-cloud interactions, which are not included in our simulations, have a strong impact on moist convection, atmospheric heating, and thus the ITCZ position, this implies that attempts to reduce ITCZ biases in prescribed-SST model setups by altering the aerosol representation will be unsuccessful. Figure 15b further shows that the ITCZ, via its impact on the hemispheric distribution of tropical clouds [Voigt et al., 2014a], is a much more potent regulator of the hemispheric-scale pattern of planetary albedo than aerosol. The persistent failure of models to simulate the observed hemispheric symmetry in planetary albedo [Voigt et al., 2013] can thus not be attributed to a misrepresentation of aerosol but instead illustrates the problems of current global models in correctly representing the ITCZ position [Voigt et al., 2014b]. Put differently, a northern model bias in the ITCZ position leads to a too bright Northern Hemisphere, and this simultaneous bias in ITCZ and planetary albedo cannot be corrected by tuning the aerosol.

The second implication concerns attempts to attribute recent ITCZ shifts to changes in anthropogenic aerosol. Recent work used the energetic framework to argue that because recent ITCZ shifts coincided with changes in aerosol, aerosol has driven these shifts [Hwang et al., 2013; Allen et al., 2015]. Our study confirms that aerosol can shift the ITCZ.

Yet the ITCZ shifts found in our simulations are small, which makes it difficult to attribute recent ITCZ shifts to changes in anthropogenic aerosol. Also, the energetic framework is a diagnostic tool that does not allow one to establish causality, in particular not in coupled simulations of the twentieth century in which several forcings evolve simultaneously, internal variability is substantial [Allen et al., 2015], model-dependent clouds influence the ITCZ shift to a degree that blurs any relation between aerosol forcing and ITCZ shift across models [Hwang et al., 2013], and ocean circulation changes mute the ITCZ response [Hawcroft et al., 2017; Kay et al., 2016]. Moreover, atmosphere models driven by observed SSTs successfully capture ITCZ shift over the second half of the twentieth century, but coupled atmosphere-ocean models fail if only aerosol is changing [Allen et al., 2015]. Thus, any attempt to attribute recent ITCZ shifts to aerosol is in fact an attempt to attribute SST changes to aerosol. This is a much more difficult task than invoking the diagnostic energetic framework.

Difficulties in attributing recent ITCZ shifts, combined with observational uncertainty and a limited time record, mean that a top-down-approach that constrains aerosol from ITCZ shifts does not seem feasible. Such a constraint might be easier to obtain from regional rainfall changes such as those related to monsoons, but even then this will require a clearer understanding of robust aerosol impacts on the circulation. We believe that this formidable challenge will much benefit from idealized aerosol prescriptions such as the one developed here and for the RFMIP simple plumes experiments of CMIP6 [Pincus et al., 2016; Stevens et al., 2017].

Appendix A: Radiation Scheme Dependence of Aerosol Atmospheric Radiative Forcing Does Not Result From Spectral Discretization or the Implementation of Aerosol Optical Depth

Section 3 identified that much of the model differences in aerosol radiative forcing, especially for the atmospheric forcing, are caused by model differences in shortwave radiative transfer schemes. One difference across the radiation schemes is the number of shortwave bands (Table A1).

LMDz5B uses the *Fouquart and Bonnell* [1980] scheme with two shortwave bands and is the most absorbing model, whereas CAM4 uses 11 bands and is the least absorbing model. This suggests that spectral resolution could be a reason for the forcing differences. Here we show, however, that this is not the case because forcing errors that could have been caused by a low number of shortwave bands were nearly eliminated by insolation-weighting of aerosol optical depth and a smart choice of the widths of the shortwave bands.

We assume that the insolation spectrum, $S(\lambda)$, is given by the Planck function for a sun emission temperature of 5778 K, and discretize $S(\lambda)$ into $n=1, 2, \dots, N$ shortwave bands of equal width that cover the wavelength range from 0.25–4.0 μm . The bands are bounded by the lower and upper wavelengths λ_n^1 and λ_n^2 , where $\lambda_n^1 < \lambda_n^2$. The insolation present in band n is

$$S_n = \frac{1}{\lambda_n^2 - \lambda_n^1} \int_{\lambda_n^1}^{\lambda_n^2} S(\lambda) d\lambda.$$

There are two possibilities to implement aerosol optical depth in a band n , τ_n . The first possibility is to define τ_n as the aerosol optical depth at the band's central wavelength, $\lambda_n^c = \frac{1}{2}(\lambda_n^1 + \lambda_n^2)$, using the Angstrom coefficient α and equation (4),

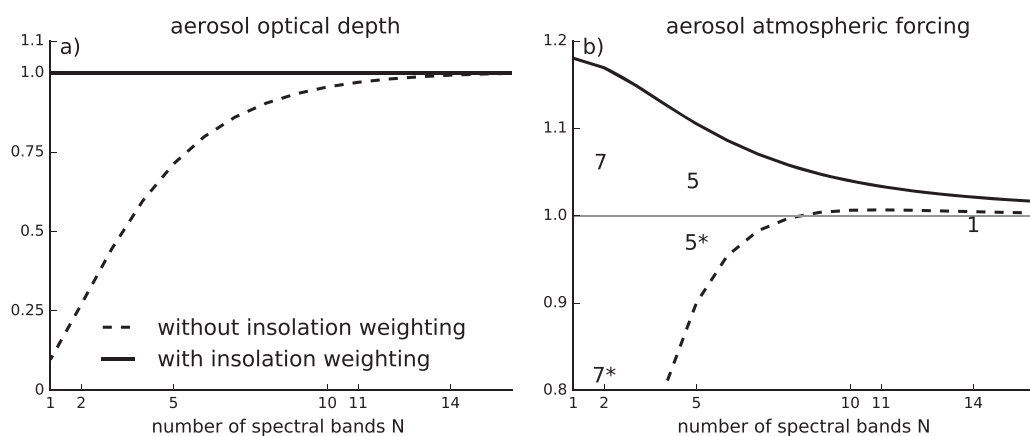


Figure A1. Theoretical estimate of the dependence of spectrally integrated total atmospheric optical depth $\bar{\tau}$ (a) and aerosol atmospheric forcing F_a (b) on the number of shortwave bands used to discretize the shortwave spectrum. The impact of insolation weighting is shown by the dashed versus solid lines. Values are normalized to the most finely resolved case, which uses $N = 200$ equally spaced spectral bands between 0.25 and 4 μm . In Figure A1b, the numbers show the estimates for the models ECHAM6 (number 1), HADGem3-A (number 5), and LMDz5B (number 7) for which the models' actual spectral bands are used; these are not equally spaced. The stars indicate the atmospheric forcing that would result if LMDz5B and HADGem3-A had not included insolation-weighting for aerosol optical depth.

AQ6

Table A1. Shortwave Radiative Transfer Schemes Employed by the Participating Models

	Model	Radiation Scheme	Number of Bands
1	ECHAM6	RRTM-G [Iacono et al., 2008]	14
2	ECHAM6-Tiedtke	RRTM-G [Iacono et al., 2008]	14
3	CAM5	RRTM-G [Iacono et al., 2008]	14
4	BCC	BCC-RAD [Zhang et al., 2014]	9
5	HADGem3-A	Edwards and Slingo [1996]	5
6	CAM4	Same as in CAM3 [Collins et al., 2006; Briegleb, 1992]	11
7	LMDz5B	Fouquart and Bonnell [1980]	2

$$\tau_n^{nw} = \tau \left(\frac{\lambda_n^c [\text{nm}]}{550 \text{ nm}} \right)^{-\alpha}$$

τ is the midvisible AOD at 550 nm. This implementation was used in all models but LMDz5B and HADGem3-A. The latter two models employed the second possibility and implemented an insolation-weighted aerosol optical depth,

$$\tau_n^{iw} = \frac{1}{S_n} \int_{\lambda_n^1}^{\lambda_n^2} \tau(\lambda) S(\lambda) d\lambda = \frac{1}{S_n} \int_{\lambda_n^1}^{\lambda_n^2} \tau \left(\frac{\lambda [\text{nm}]}{550 \text{ nm}} \right)^{-\alpha} S(\lambda) d\lambda.$$

The superscripts nw and iw indicate whether a spectral band's τ_n is defined with insolation weighting (iw) or without (nw). With this, the aerosol optical depth averaged over all wavelengths is

$$\bar{\tau}^{nw/iw} = \frac{\sum_n \tau_n^{nw/iw} S_n}{\sum_n S_n}. \tag{A1}$$

Neglecting reflection inside the atmosphere and at the surface, aerosol-induced atmospheric absorption scales with $1 - e^{-\tau}$, and so integrated over the solar spectrum the atmospheric aerosol radiative forcing scales as

$$F_a^{nw/iw} \propto \frac{\sum_n (1 - e^{-\tau_n^{nw/iw}}) S_n}{\sum_n S_n}. \tag{A2}$$

To quantify the impact of spectral resolution and insolation-weighting on $F_a^{nw/iw}$, we numerically solve equations (A1) and (A2) as a function of the number of equally wide shortwave bands, N . Figure Figure A1 shows the result of this computation. Insolation-weighting makes aerosol optical depth insensitive to N (solid line in Figure A1a). For F_a insolation-weighting has little effect if $N \geq 10$, justifying that it was not applied in ECHAM6, ECHAM6-Tiedtke, CAM5, BCC, and CAM4. For smaller N , however, insolation-weighting is important as otherwise $\bar{\tau}$ (dashed line in Figure A1a) and F_a (dashed line in Figure A1b) would be underestimated by several tens of percent. This shows that in the two models with the least number of spectral bands, LMDz5B ($N = 2$) and HADGem3-A ($N = 5$), the use of insolation weighting helps to alleviate the impact of spectral resolution.

Nevertheless, even with insolation-weighting, F_a can substantially depend on spectral resolution (solid line in Figure A1b). As N decreases, F_a increases. If $N = 2$ and $N = 5$ equally wide shortwave bands were used, F_a would be overestimated by 18 and 10%, respectively. However, LMDz5B and HADGem3-A use spectral bands with nonequal widths that are based on the shape of $S(\lambda)$, and this further reduces the impact of spectral resolution to a few percent (symbols 7 and 5 in Figure A1b). Model differences in radiative transfer schemes thus cannot be explained as the result of differences in spectral resolution. This can also be seen from the fact that models differ in F_a even for $N \geq 10$ (Figure 7b).

Acknowledgments

This work contributes to the WCRP Grand Challenge on Clouds, Circulation, and Climate Sensitivity. A.V. received partial support from the German Science Foundation under grant agreement DFG-VO 1765/3-1 and from the German Ministry of Education and Research (BMBF) and FONa: Research for Sustainable Development (www.fona.de) under grant agreement 01LK1509A. R.P. appreciates support from the Regional and Global Climate Modeling Program of the US Department of Energy Office of Environmental and Biological Sciences under grant DE-SC0012549, and from the National Science Foundation Science and Technology Center for Multi-Scale Modeling of Atmospheric Processes, managed by Colorado State University under cooperative agreement ATM-0425247. B.M. acknowledges support from the Regional and Global Climate Modeling Program of the U.S. Department of Energy's Office of Science, Cooperative agreement DE-FC02-97ER62402. The ECHAM6 simulations were carried out at the German Climate Computing Center (DKRZ). The GPCP combined precipitation data were developed and computed by the NASA/Goddard Space Flight Center's Laboratory for Atmospheres as a contribution to the GEWEX Global Precipitation Climatology Project. The GPCP data used in this paper were provided by the NOAA/OAR/ESRL PSD, Boulder, Colorado, USA, from their website at <http://www.esrl.noaa.gov/psd/>. NCAR is sponsored by the National Science Foundation. The Easy Aerosol simulations are available from AV upon request.

References

- Adler, R., et al. (2003), The version-2 global precipitation climatology project (GPCP) monthly precipitation analysis (1979-present), *J. Hydro-meteorol.*, *4*(6), 1147–1167, doi:10.1175/1525-7541(2003)004<1147:TVGPCP>2.0.CO;2.
- Allen, M. R., and W. J. Ingram (2002), Constraints on future changes in climate and the hydrologic cycle, *Nature*, *419*, 224–232, doi:10.1038/nature01092.
- Allen, R. J. (2015), A 21st century northward tropical precipitation shift caused by future anthropogenic aerosol reductions, *J. Geophys. Res. Atmos.*, *120*, 9087–9102, doi:10.1002/2015JD023623.
- Allen, R. J., and S. C. Sherwood (2011), The impact of natural versus anthropogenic aerosols on atmospheric circulation in the Community Atmosphere Model, *Clim. Dyn.*, *36*, 1959–1978, doi:10.1007/s00382-010-0898-8.
- Allen, R. J., A. T. Evan, and B. B. Booth (2015), Interhemispheric aerosol radiative forcing and tropical precipitation shifts during the late twentieth century, *J. Clim.*, *28*(20), 8219–8246, doi:10.1175/JCLI-D-15-0148.1.
- Andrews, T., P. M. Forster, O. Boucher, N. Bellouin, and A. Jones (2010), Precipitation, radiative forcing and global temperature change, *Geophys. Res. Lett.*, *37*, L14701, doi:10.1029/2010GL043991.
- Bentsen, M., et al. (2013), The Norwegian earth system model, noresm1-m—part 1: Description and basic evaluation of the physical climate, *Geosci. Model Dev.*, *6*(3), 687–720, doi:10.5194/gmd-6-687-2013.
- Bollasina, M. A., Y. Ming, and V. Ramaswamy (2011), Anthropogenic aerosols and the weakening of the south Asian summer monsoon, *Science*, *334*, 502–505, doi:10.1126/science.1204994.
- Bony, S., G. Bellon, D. Klocke, S. Sherwood, S. Fermepin, and S. Denvil (2013), Robust direct effect of carbon dioxide on tropical circulation and regional precipitation, *Nat. Geosci.*, *6*, 447–451, doi:10.1038/ngeo1799.
- Boucher, O., et al. (1998), Intercomparison of models representing direct shortwave radiative forcing by sulfate aerosols, *J. Geophys. Res.*, *103*(D14), 16,979–16,998, doi:10.1029/98JD00997.
- Boucher, O., et al. (2013), Clouds and aerosols, in *Climate Change 2013: The Physical Science Basis. Contribution of Working Group I to the Fifth Assessment Report of the Intergovernmental Panel on Climate Change*, edited by T. Stocker et al., Cambridge Univ. Press, Cambridge, U. K.
- Briegleb, B. P. (1992), Delta-Eddington approximation for solar radiation in the NCAR Community Climate Model, *J. Geophys. Res.*, *97*(D7), 7603–7612.
- Butler, A. H., D. W. J. Thompson, and R. Heikes (2010), The steady-state atmospheric circulation response to climate change-like thermal forcings in a simple general circulation model, *J. Clim.*, *23*, 3474–3496, doi:10.1175/2010JCLI3228.1.
- Ceppi, P., M. D. Zelinka, and D. L. Hartmann (2014), The response of the Southern Hemispheric Eddy-driven jet to future changes in shortwave radiation in CMIP5, *Geophys. Res. Lett.*, *41*, 3244–3250, doi:10.1002/2014GL060043.
- Collins, W. D., P. J. Rasch, B. A. Boville, J. J. Hack, J. R. McCaa, D. L. Williamson, B. P. Briegleb, C. M. Bitz, S.-J. Lin, and M. Zhang (2006), The formulation and atmospheric simulation of the Community Atmosphere Model version 3 (CAM3), *J. Clim.*, *19*(11), 2144–2161, doi:10.1175/JCLI3760.1.
- DeAngelis, A. M., X. Qu, M. D. Zelinka, and A. Hall (2015), An observational radiative constraint on hydrologic cycle intensification, *Nature*, *528*(7581), 249–253, doi:10.1038/nature15770.
- Donohoe, A., J. Marshall, D. Ferreira, and D. Mcgee (2013), The relationship between ITCZ location and cross-equatorial atmospheric heat transport: From the seasonal cycle to the last glacial maximum, *J. Clim.*, *26*(11), 3597–3618, doi:10.1175/JCLI-D-12-00467.1.
- Edwards, J. M., and A. Slingo (1996), Studies with a flexible new radiation code. I: Choosing a configuration for a large-scale model, *Q. J. R. Meteorol. Soc.*, *122*, 689–719, doi:10.1002/qj.49712253107.
- Fläschner, D., T. Mauritsen, and B. Stevens (2016), Understanding the intermodel spread in global-mean hydrological sensitivity, *J. Clim.*, *29*(2), 801–817, doi:10.1175/JCLI-D-15-0351.1.
- Fouquart, Y., and B. Bonnell (1980), Computations of solar heating of the Earth's atmosphere, *Beitr. Phys. Atmos.*, *53*, 35–62.
- Friedman, A. R., Y.-T. Hwang, J. C. H. Chiang, and D. M. W. Frierson (2013), Interhemispheric temperature asymmetry over the twentieth century and in future projections, *J. Clim.*, *26*(15), 5419–5433, doi:10.1175/JCLI-D-12-00525.1.
- Frierson, D. M. W., and Y.-T. Hwang (2012), Extratropical influence on ITCZ shifts in slab ocean simulations of global warming, *J. Clim.*, *25*, 720–730.
- Gates, W. L. (1992), AMIP: The atmospheric model intercomparison project, *Bull. Am. Meteorol. Soc.*, *73*(12), 1962–1970, doi:10.1175/1520-0477(1992)073<1962:ATAMIP>2.0.CO;2.
- Hawcroft, M., J. M. Haywood, M. Collins, A. Jones, A. C. Jones, and G. Stephens (2017), Southern Ocean albedo, inter-hemispheric energy transports and the double ITCZ: Global impacts of biases in a coupled model, *Clim. Dyn.*, *48*, 2279–2295.
- Haywood, J. M., A. Jones, N. Bellouin, and D. Stephenson (2013), Asymmetric forcing from stratospheric aerosols impacts Sahelian rainfall, *Nat. Clim. Change*, *3*(7), 660–665, doi:10.1038/NCLIMATE1857.
- Hewitt, H. T., D. Copey, I. D. Culverwell, C. M. Harris, R. S. R. Hill, A. B. Keen, A. J. McLaren, and E. C. Hunke (2011), Design and implementation of the infrastructure of HadGEM3: The next-generation Met Office climate modelling system, *Geosci. Model Dev.*, *4*(2), 223–253, doi:10.5194/gmd-4-223-2011.
- Hill, S. A., Y. Ming, and I. M. Held (2015), Mechanisms of forced tropical meridional energy flux change, *J. Clim.*, *28*(5), 1725–1742, doi:10.1175/JCLI-D-14-00165.1.
- Hourdin, F., et al. (2013), LMDZ5B: the atmospheric component of the IPSL climate model with revisited parameterizations for clouds and convection, *Clim. Dyn.*, *40*, 2193–2222, doi:10.1007/s00382-012-1343-y.
- Hwang, Y.-T., D. M. W. Frierson, and S. M. Kang (2013), Anthropogenic sulfate aerosol and the southward shift of tropical precipitation in the late 20th century, *Geophys. Res. Lett.*, *40*, 2845–2850, doi:10.1002/grl.50502.
- Iacono, M. J., J. S. Delamere, E. J. Mlawer, M. W. Shephard, S. A. Clough, and W. D. Collins (2008), Radiative forcing by long-lived greenhouse gases: Calculations with the AER radiative transfer models, *J. Geophys. Res.*, *113*, D13103, doi:10.1029/2008JD009944.
- Kang, S. M., I. M. Held, D. M. W. Frierson, and M. Zhao (2008), The response of the ITCZ to extratropical thermal forcing: Idealized slab-ocean experiments with a GCM, *J. Clim.*, *21*, 3521–3532, doi:10.1175/2007JCLI2146.1.
- Kang, S. M., D. M. W. Frierson, and I. M. Held (2009), The tropical response to extratropical thermal forcing in an idealized GCM: The importance of radiative feedbacks and convective parameterization, *J. Atmos. Sci.*, *66*, 2812–2827, doi:10.1175/2009JAS2924.1.
- Kasoar, M., A. Voulgarakis, J.-F. Lamarque, D. T. Shindell, N. Bellouin, W. J. Collins, G. Faluvegi, and K. Tsigaridis (2016), Regional and global climate response to anthropogenic SO₂ emissions from China in three climate models, *Atmos. Chem. Phys.*, *16*, 9785–9804, doi:10.5194/acp-16-9785-2016.
- Kato, S., N. G. Loeb, F. G. Rose, D. R. Doelling, D. A. Rutan, T. E. Caldwell, L. Yu, and R. A. Weller (2013), Surface irradiances consistent with CERES-derived top-of-atmosphere shortwave and longwave irradiances, *J. Clim.*, *26*(9), 2719–2740, doi:10.1175/JCLI-D-12-00436.1.

- Kay, J. E., C. Wall, V. Yettella, B. Medeiros, C. Hannay, P. Caldwell, and C. Bitz (2016), Global climate impacts of fixing the southern ocean shortwave radiation bias in the community earth system model (CESM), *J. Clim.*, *29*(12), 4617–4636, doi:10.1175/JCLI-D-15-0358.1.
- Kinne, S., D. O'Donnel, P. Stier, S. Kloster, K. Zhang, H. Schmidt, S. Rast, M. Giorgetta, T. F. Eck, and B. Stevens (2013), Mac-v1: A new global aerosol climatology for climate studies, *J. Adv. Model. Earth Syst.*, *5*, 704–740, doi:10.1002/jame.20035.
- Loeb, N. G., B. A. Wielicki, D. R. Doelling, G. L. Smith, D. F. Keyes, S. Kato, N. Manalo-Smith, and T. Wong (2009), Toward optimal closure of the Earth's top-of-atmosphere radiation budget, *J. Clim.*, *22*(3), 748–766, doi:10.1175/2008JCLI2637.1.
- Meehl, G. A., J. M. Arblaster, and W. D. Collins (2008), Effects of black carbon aerosols on the Indian monsoon, *J. Clim.*, *21*(12), 2869–2882, doi:10.1175/2007JCLI1777.1.
- Ming, Y., and V. Ramaswamy (2011), A model investigation of aerosol-induced changes in tropical circulation, *J. Clim.*, *21*, 5125–5133, doi:10.1175/2011JCLI4108.1.
- Möbis, B., and B. Stevens (2012), Factors controlling the position of the ITCZ on an Aquaplanet, *J. Adv. Model. Earth Syst.*, *4*, M00A04, doi:10.1029/2012MS000199.
- Myhre, G., et al. (2013), Radiative forcing of the direct aerosol effect from AeroCom Phase II simulations, *Atmos. Chem. Phys.*, *13*(4), 1853–1877, doi:10.5194/acp-13-1853-2013.
- Neale, R. B., et al. (2010), Description of the NCAR Community Atmosphere Model (CAM 5.0), *Tech. Note NCAR/TN-486+STR*, NCAR, Boulder, Colo.
- Neale, R. B., J. Richter, S. Park, P. H. Lauritzen, S. J. Vavrus, P. J. Rasch, and M. Zhang (2013), The mean climate of the Community Atmosphere Model (CAM4) in forced SST and fully coupled experiments, *J. Clim.*, *26*(14), 5150–5168, doi:10.1175/JCLI-D-12-00236.1.
- Ocko, I. B., V. Ramaswamy, and Y. Ming (2014), Contrasting climate responses to the scattering and absorbing features of anthropogenic aerosol forcings, *J. Clim.*, *27*(14), 5329–5345, doi:10.1175/JCLI-D-13-00401.1.
- Park, S., C. S. Bretherton, and P. J. Rasch (2014), Integrating cloud processes in the Community Atmosphere Model, Version 5, *J. Clim.*, *27*(18), 6821–6856, doi:10.1175/JCLI-D-14-00087.1.
- Pincus, R., et al. (2015), Radiative flux and forcing parameterization error in aerosol-free clear skies, *Geophys. Res. Lett.*, *42*, 5485–5492, doi:10.1002/2015GL064291.
- Pincus, R., P. M. Forster, and B. Stevens (2016), The radiative forcing model intercomparison project (RFMIP): Experimental protocol for CMIP6, *Geosci. Model Dev. Discuss.*, *2016*, 1–18, doi:10.5194/gmd-2016-88.
- Randles, C. A., et al. (2013), Intercomparison of shortwave radiative transfer schemes in global aerosol modeling: Results from the AeroCom radiative transfer experiment, *Atmos. Chem. Phys.*, *13*(5), 2347–2379, doi:10.5194/acp-13-2347-2013.
- Ridley, H. E., et al. (2015), Aerosol forcing of the position of the intertropical convergence zone since AD 1550, *Nat. Geosci.*, *8*(3), 195–200, doi:10.1038/NGEO2353.
- Seo, J., S. M. Kang, and T. M. Merlis (2017), A model intercomparison of the tropical precipitation response to a CO₂ doubling in aquaplanet simulations, *Geophys. Res. Lett.*, *44*, 993–1000, doi:10.1002/2016GL072347.
- Shaw, T. A., and A. Voigt (2015), Tug of war on summertime circulation between radiative forcing and sea surface warming, *Nat. Geosci.*, *8*(7), 560–566, doi:10.1038/ngeo2449.
- Shaw, T. A., A. Voigt, S. Kang, and J. Seo (2015), Response of the intertropical convergence zone to zonally-asymmetric subtropical surface forcings, *Geophys. Res. Lett.*, *42*, 9961–9969, doi:10.1002/2015GL066027.
- Sherwood, S. C., S. Bony, O. Boucher, C. Bretherton, P. M. Forster, J. M. Gregory, and B. Stevens (2015), Adjustments in the forcing-feedback framework for understanding climate change, *Bull. Am. Meteorol. Soc.*, *96*(2), 217–228, doi:10.1175/BAMS-D-13-00167.1.
- Stevens, B., et al. (2013), Atmospheric component of the MPI-M Earth System Model: ECHAM6, *J. Adv. Model. Earth Syst.*, *5*, 146–172, doi:10.1002/jame.20015.
- Stevens, B., S. Fiedler, S. Kinne, K. Peters, S. Rast, J. Müsse, S. J. Smith, and T. Mauritsen (2017), MACv2-SP: A parameterization of anthropogenic aerosol optical properties and an associated Twomey effect for use in CMIP6, *Geosci. Model Dev.*, *10*, 433–452, doi:10.5194/gmd-10-433-2017.
- Stier, P., et al. (2013), Host model uncertainties in aerosol radiative forcing estimates: Results from the aerocom prescribed intercomparison study, *Atmos. Chem. Phys.*, *13*, 3245–3270, doi:10.5194/acp-13-3245-2013.
- Taylor, K. E., R. J. Stouffer, and G. A. Meehl (2012), An overview of CMIP5 and the experiment design, *Bull. Am. Meteorol. Soc.*, *93*, 485–498, doi:10.1175/BAMS-D-11-00094.1.
- Toohey, M., B. Stevens, H. Schmidt, and C. Timmreck (2016), Easy volcanic aerosol (EVA v1.0): An idealized forcing generator for climate simulations, *Geosci. Model Dev.*, *9*(11), 4049–4070, doi:10.5194/gmd-9-4049-2016.
- Voigt, A., and T. Shaw (2015), Circulation response to warming shaped by radiative changes of clouds and water vapor, *Nat. Geosci.*, *8*, 102–106, doi:10.1038/ngeo2345.
- Voigt, A., B. Stevens, J. Bader, and T. Mauritsen (2013), The observed hemispheric symmetry in reflected shortwave irradiance, *J. Clim.*, *26*, 468–477, doi:10.1175/JCLI-D-12-00132.1.
- Voigt, A., S. Bony, J.-L. Dufresne, and B. Stevens (2014a), Radiative impact of clouds on the shift of the intertropical convergence zone, *Geophys. Res. Lett.*, *41*, 4308–4315, doi:10.1002/2014GL060354.
- Voigt, A., B. Stevens, J. Bader, and T. Mauritsen (2014b), Compensation of hemispheric albedo asymmetries by shifts of the ITCZ and tropical clouds, *J. Clim.*, *27*, 1029–1045, doi:10.1175/JCLI-D-13-00205.1.
- Woelfle, M. D., C. S. Bretherton, and D. M. W. Frierson (2015), Time scales of response to antisymmetric surface fluxes in an aquaplanet GCM, *Geophys. Res. Lett.*, *42*, 2555–2562, doi:10.1002/2015GL063372.
- Wu, T., R. Yu, F. Zhang, Z. Wang, M. Dong, L. Wang, X. Jin, D. Chen, and L. Li (2010), The Beijing Climate Center atmospheric general circulation model: Description and its performance for the present-day climate, *Clim. Dyn.*, *34*(1), 123–147, doi:10.1007/s00382-008-0487-2.
- Xie, S.-P., B. Lu, and B. Xiang (2013), Similar spatial patterns of climate responses to aerosol and greenhouse gas changes, *Nat. Geosci.*, *6*(10), 828–832, doi:10.1038/NGEO1931.
- Yoshimori, M., and A. J. Broccoli (2008), Equilibrium response of an atmosphere mixed layer ocean model to different radiative forcing agents: Global and zonal mean response, *J. Clim.*, *21*, 4399–4423, doi:10.1175/2008JCLI2172.1.
- Yoshimori, M., and A. J. Broccoli (2009), On the link between Hadley circulation changes and radiative feedback processes, *Geophys. Res. Lett.*, *36*, L20703, doi:10.1029/2009GL040488.
- Zhang, H., X. W. Jing, and J. Li (2014), Application and evaluation of a new radiation code under mcICA scheme in BCC_AGCM2.0.1, *Geosci. Model Dev.*, *7*, 737–754, doi:10.5194/gmd-7-737-2014.